Engineering Analysis Studies for Preliminary Design of Lightweight Cryogenic Hydrogen Tanks in UAV Applications

Roy M. Sullivan
Glenn Research Center, Cleveland, Ohio

Joseph L. Palko
Connecticut Reserve Technologies, Inc., Strongsville, Ohio

Robert T. Tornabene
Glenn Research Center, Cleveland, Ohio

Brett A. Bednarcyk and Lynn M. Powers
Ohio Aerospace Institute, Brook Park, Ohio

Subodh K. Mital
University of Toledo, Toledo, Ohio

Lizalyn M. Smith, Xiao-Yen J. Wang, and James E. Hunter
Glenn Research Center, Cleveland, Ohio

NASA STI Program . . . in Profile

Since its founding, NASA has been dedicated to the advancement of aeronautics and space science. The NASA Scientific and Technical Information (STI) program plays a key part in helping NASA maintain this important role.

The NASA STI Program operates under the auspices of the Agency Chief Information Officer. It collects, organizes, provides for archiving, and disseminates NASA's STI. The NASA STI program provides access to the NASA Aeronautics and Space Database and its public interface, the NASA Technical Reports Server, thus providing one of the largest collections of aeronautical and space science STI in the world. Results are published in both non-NASA channels and by NASA in the NASA STI Report Series, which includes the following report types:

- TECHNICAL PUBLICATION. Reports of completed research or a major significant phase of research that present the results of NASA programs and include extensive data or theoretical analysis. Includes compilations of significant scientific and technical data and information deemed to be of continuing reference value. NASA counterpart of peer-reviewed formal professional papers but has less stringent limitations on manuscript length and extent of graphic presentations.

- TECHNICAL MEMORANDUM. Scientific and technical findings that are preliminary or of specialized interest, e.g., quick release reports, working papers, and bibliographies that contain minimal annotation. Does not contain extensive analysis.

- CONTRACTOR REPORT. Scientific and technical findings by NASA-sponsored contractors and grantees.

- CONFERENCE PUBLICATION. Collected papers from scientific and technical conferences, symposia, seminars, or other meetings sponsored or cosponsored by NASA.

- SPECIAL PUBLICATION. Scientific, technical, or historical information from NASA programs, projects, and missions, often concerned with subjects having substantial public interest.

- TECHNICAL TRANSLATION. English-language translations of foreign scientific and technical material pertinent to NASA's mission.

Specialized services also include creating custom thesauri, building customized databases, organizing and publishing research results.

For more information about the NASA STI program, see the following:

- Access the NASA STI program home page at *http://www.sti.nasa.gov*

- E-mail your question via the Internet to *help@sti.nasa.gov*

- Fax your question to the NASA STI Help Desk at 301–621–0134

- Telephone the NASA STI Help Desk at 301–621–0390

- Write to:
  NASA STI Help Desk
  NASA Center for AeroSpace Information
  7121 Standard Drive
  Hanover, MD 21076–1320

Engineering Analysis Studies for Preliminary Design of Lightweight Cryogenic Hydrogen Tanks in UAV Applications

Roy M. Sullivan
Glenn Research Center, Cleveland, Ohio

Joseph L. Palko
Connecticut Reserve Technologies, Inc., Strongsville, Ohio

Robert T. Tornabene
Glenn Research Center, Cleveland, Ohio

Brett A. Bednarcyk and Lynn M. Powers
Ohio Aerospace Institute, Brook Park, Ohio

Subodh K. Mital
University of Toledo, Toledo, Ohio

Lizalyn M. Smith, Xiao-Yen J. Wang, and James E. Hunter
Glenn Research Center, Cleveland, Ohio

National Aeronautics and
Space Administration

Glenn Research Center
Cleveland, Ohio 44135

May 2006

Acknowledgments

Level of Review: This material has been technically reviewed by an expert single reviewer.

Available from

NASA Center for Aerospace Information
7121 Standard Drive
Hanover, MD 21076–1320

National Technical Information Service
5285 Port Royal Road
Springfield, VA 22161

Available electronically at http://gltrs.grc.nasa.gov

Engineering Analysis Studies for Preliminary Design of Lightweight Cryogenic Hydrogen Tanks in UAV Applications

Roy M. Sullivan
National Aeronautics and Space Administration
Glenn Research Center
Cleveland, Ohio 44135

Joseph L. Palko
Connecticut Reserve Technologies, Inc.
Strongsville, Ohio 44136

Robert T. Tornabene
National Aeronautics and Space Administration
Glenn Research Center
Cleveland, Ohio 44135

Brett A. Bednarcyk and Lynn M. Powers
Ohio Aerospace Institute
Brook Park, Ohio 44142

Subodh K. Mital
University of Toledo
Toledo, Ohio 43606

Lizalyn M. Smith, Xiao-Yen J. Wang, and James E. Hunter
National Aeronautics and Space Administration
Glenn Research Center
Cleveland, Ohio 44135

Summary

A series of engineering analysis studies were conducted to investigate the potential application of nanoclay-enhanced graphite/epoxy composites and polymer cross-linked silica aerogels in cryogenic hydrogen storage tank designs. This assessment focused on the application of these materials in spherical tank designs for unmanned aeronautic vehicles with mission durations of 14 days. Two cryogenic hydrogen tank design concepts were considered: a vacuum-jacketed design and a sandwiched construction with an aerogel insulating core. Analyses included thermal and structural analyses of the tank designs as well as an analysis of hydrogen diffusion to specify the material permeability requirements. The analyses also provided material property targets for the continued development of cross-linked aerogels and nanonclay-enhanced graphite/epoxy composites for cryogenic storage tank applications. The results reveal that a sandwiched construction with an aerogel core is not a viable design solution for a 14-day mission. A vacuum-jacketed design approach was shown to be far superior to an aerogel. Aerogel insulation may be feasible for shorter duration missions. The results also reveal that the application of nanoclay-enhanced graphite/epoxy should be limited to the construction of outer tanks in a vacuum-jacketed design, since a graphite/epoxy inner tank does not provide a significant weight savings over aluminum and since the ability of nanoclay-enhanced graphite/epoxy to limit hydrogen permeation is still in question.

Introduction

Unmanned aeronautic vehicles (UAVs) are a proven asset in tactical military applications, providing remotely operated surveillance and reconnaissance capability in battlefield operations (ref. 1). The Predator, for example, is a medium-altitude, long-endurance vehicle that provides surveillance and target acquisition, in addition to conducting armed reconnaissance against critical, perishable targets. The Global Hawk is a high-altitude vehicle capable of providing near-real-time high-resolution intelligence, surveillance, and reconnaissance imagery to battlefield commanders.

The civilian aviation sector envisions an extensive role for UAVs in the coming decades (ref. 2). One arena where UAVs may provide a significant benefit is in atmospheric science research. UAVs are being proposed as sensing platforms for a variety of atmospheric science missions including hurricane

tracking and monitoring, cloud formation studies, and the analysis of forest fire plume constituents (ref. 2). UAVs offer the advantage of close-range sensing capability without jeopardizing human lives during hazardous atmospheric science missions. Many of these atmospheric science missions require high-altitude long-endurance platforms, necessitating the development of UAVs with low vehicle dry weight. In addition, there is also the desire to develop such vehicles as environmentally friendly aircraft. As such, the development of lightweight, reliable hydrogen storage tank design concepts has been identified as an area of research focus.

Over the last few years, the National Aeronautics and Space Administration has invested a moderate amount of resources into the development of cross-linked silica aerogels and nanoclay-enhanced graphite/epoxy composites with the idea that these materials may provide considerable benefit for the design of advanced lightweight durable tank designs. Nanoclay-enhanced graphite/epoxy composites are made by adding clay platelets to the epoxy prior to fiber impregnation. The addition of the clay platelets should decrease the composite material's permeability by decreasing the permeability of the epoxy matrix and by increasing the toughness and lowering the thermal expansion coefficient of the epoxy matrix. The latter two effects will reduce the amount of matrix cracking, which results from cryogenic thermal cycling and the thermal expansion mismatch between the fibers and epoxy matrix. Nanoclay-enhanced graphite/epoxy has been proposed as a material candidate for cryogenic tanks, as it may offer a possible weight reduction over metal tanks and may provide sufficient hydrogen permeation resistance.

Silica aerogels are solid materials with extremely low density and low thermal conductivity. Unfortunately, they have very limited strength. They possess tensile strengths less than a few pounds per square inch (ref. 3). The addition of polymers to reinforce the links between secondary silica particles provides a significant increase in strength. Cross-linked silica aerogels have been proposed as a lightweight, durable insulation candidate. The properties of the cross-linked silica aerogels can be tailored by modifications to the formulation, but to obtain higher strengths, the desirable properties such as low density and low thermal conductivity must be sacrificed.

It is prudent at this juncture to perform some engineering analysis calculations to determine the possibility of using these materials in UAV tank applications and to obtain a quantitative assessment of their benefits. In addition, these engineering analysis studies can be used to set material property value targets for the continued development of these materials for tank applications. This paper reports on the engineering analysis studies. The analysis methods that were employed are described, and the results from these analyses are presented.

In order to investigate the application of cross-linked silica aerogels and nanoclay-enhanced graphite/epoxy composites in cryogenic hydrogen tank designs, two tank design approaches

were considered: (1) a vacuum-jacketed tank design and (2) a sandwiched tank construction consisting of an inner and outer shell and an aerogel insulating core. Using a common set of tank design specifications, thermal and structural analyses of each design were performed.

In the first section of this report, the ability of the aerogel to provide sufficient thermal insulation during a 14-day mission was examined. The thermal insulating efficiency of the cross-linked aerogel insulation was compared to that of a vacuum jacket approach as well as that of spray-on foam insulation. The vacuum jacket approach was examined with and without a multilayer insulation (MLI) blanket. Also, two cross-linked aerogels were considered: a low-density aerogel with low thermal conductivity and low strength and a higher density aerogel with a higher conductivity and a higher strength.

After that, the results of the structural analysis of the vacuum-jacketed tank design are reported. The results of the structural analysis help to size the tank wall thickness and provide an estimate of the tank weight. Both aluminum and graphite/epoxy composites were considered as possible candidates for the inner tank construction. Aluminum, steel, and graphite/epoxy were considered candidates for the outer tank. In addition, various construction approaches were considered for the outer tank. The analyses presented here are not intended to represent detailed design analyses for the purpose of qualifying hardware for flight certification, but rather a series of analyses on preliminary design concepts for the purpose of estimating potential weight savings with the use of nanoclay-enhanced graphite/epoxy composites.

Next, the results of the sandwiched tank design assessment are reported. The structural analysis was performed assuming a cross-linked silica aerogel insulation core with inner and outer shells fabricated from nanoclay-enhanced graphite/epoxy. Structural analysis of the sandwiched design with an aerogel core under a variety of possible load combinations was performed in order to obtain an estimate of the aerogel stress magnitudes expected in operation.

In the final section, the issue of the nanoclay-enhanced graphite/epoxy material permeability is addressed. In either the vacuum-jacketed design or the sandwiched aerogel core design, permeation through the graphite/epoxy walls may jeopardize the ability of the tank design to perform its intended function. The relation between the material permeability and the rate of pressurization in the space between the inner and outer walls is determined using Darcy's law and the ideal gas law. By restricting the rate of pressurization to an acceptable level, the maximum allowable material permeability can be established.

While reading this report, the reader may notice some slight inconsistencies between the sections of this report. For instance, while performing the thermal and structural analysis of the inner tank in a vacuum-jacketed design, the analysis tools used for the aluminum tank were not the same tools used to analyze the graphite/epoxy design. In addition, some of the thermal boundary conditions imposed on the aluminum tank are not identical to those imposed on the graphite/epoxy tank.

Another example is that the analysis to assess an aluminum inner tank design included the outer tank whereas the analysis of the graphite/epoxy inner tank did not. The analyses that are described in this report were performed by a team of analysts; each analysis task was performed by a different team member. Every attempt has been made to assemble these analyses into a logical and seamless report. However, the reader must keep in mind that two analysts do not always approach the same problem in two identical manners. There are other inconsistencies between the various sections; however, these inconsistencies have little or no impact on the conclusions drawn from the results of these analyses.

Tank Design Specifications and Requirements

The primary ground rule that was imposed was to perform preliminary design trade studies assuming the storage tank application is for a UAV designed for a 14-day mission duration and an altitude of 65 000 ft. In addition, the preliminary design studies would be performed assuming a spherical propellant storage tank or tanks.

During the course of this tank design effort, two separate parallel efforts were also pursued: one involved trade studies for the preliminary design of the vehicle (Yetter, J., et al.: High Altitude Long Endurance (HALE) Remotely Operated Aircraft (ROA) Capabilities and Technology Needs for Earth and Space Science Research. 2006, to be published as NASA TM), and the other focused on hydrogen delivery system trade studies (Millis, M.G., et al.: Design Trades for Hydrogen Fueled Remotely Operated Aircraft. 2006, to be published as NASA TM). The hydrogen delivery system trade studies were conducted without specifying the propulsion and power source, leaving the selection open to one of three possible systems: an internal combustion engine, a proton exchange membrane fuel cell, and a solid oxide fuel cell. Propellers driven by any one of the three would provide the vehicle thrust. The preliminary vehicle design studies provided an estimate of the horsepower requirements to meet mission objectives. Using the horsepower requirement, the fuel consumption rates were established, and this, along with the mission duration, determined the total amount of propellant required to complete the mission. It was determined that 2645 lb of propellant would be required to meet the mission objectives (Yetter, J., et al., 2006, to be published as NASA TM). The vehicle design trade studies were performed assuming an internal combustion engine, the least efficient of the three engine choices. This yielded an upper bound on the required propellant mass.

A list of design specifications and requirements pertinent to the tank design are shown in table I. In order to keep the tank(s) a reasonable size, it is necessary to store 2645 lb of propellant in two tanks (1323 lb per tank). Assuming an ullage volume of 5 percent (Millis, M.G., et al., 2006, to be published as NASA TM), 1323 lb of liquid hydrogen would require an

8.5-ft-diameter tank. The internal pressure of 30 psi was chosen as it was considered a standard operating pressure and was deemed to be sufficient to meet the delivery system requirements (Millis, M.G., et al., 2006, to be published as NASA TM). The worst case ground operation conditions were assumed to be 14.7 psi ambient pressure and an ambient air temperature of 125 °F. The ambient air temperature and pressure conditions for altitude (–70 °F and 0.8 psi, respectively) are the environmental conditions at an altitude of 65 000 ft. The vehicle acceleration loads of 3.5g vertical and 0.5g lateral were considered typical acceleration loads for the class of flight vehicle being considered here. A structural safety factor of 1.5 was chosen as it is a fairly typical value used for aeronautics and aerospace structures. It is also consistent with the Federal Aviation Administration Regulations (FAR, ref. 4) for aircraft structural components. It should be noted, however, that the FAR does not specifically address UAVs.

TABLE I.—PRELIMINARY TANK DESIGN
SPECIFICATIONS AND REQUIREMENTS

Mission duration, days.. 14
Spherical tank diameter, ft... 8.5
Internal tank pressure, psi... 30

Ambient air temperature conditions, °F
Ground operations 125
Altitude.. –70

Ambient air pressure conditions, psi
Ground operations 14.7
Altitude... 0.8

Vehicle acceleration loads, g
Vertical... 3.5
Lateral 0.5

Structural factor of safety 1.5

Thermal Insulation Assessment: Comparison of Insulating Approaches

In an effort to assess the viability of various insulating approaches to provide an adequate thermal barrier for a 14-day mission and to compare the relative efficiencies of these schemes, a series of one-dimensional heat flow calculations were performed. The insulation approaches that were considered are a vacuum-jacketed tank utilizing a multilayer insulation (MLI) blanket in the vacuum gap, a vacuum-jacketed design with no MLI, a single-walled tank utilizing external spray on foam insulation (SOFI), a single-walled tank utilizing high-density, high-strength aerogel insulation, and a single-walled tank utilizing low-density, low-strength aerogel insulation. High- and low-density aerogels with and without vacuum were considered.

The heat flow calculations were performed for each of the candidate thermal insulation approaches and for a variety of assumed insulation thicknesses. The calculations were based on the one-dimensional Fourier heat conduction equation for all insulation approaches except for the vacuum jacket without a MLI blanket. With that approach, radiation heat transfer was assumed. The assumed boundary conditions are cryogenic hydrogen temperatures at the inner surface and –70 °F ambient air temperature on the exterior. Each heat flow calculation yields a rate of heat penetration into the tank. The rate of liquid hydrogen boiloff was calculated from the heat penetration rates and the heat of vaporization. This resulted in an estimate of the rate of liquid hydrogen boiloff for each insulation approach and for each assumed insulation thickness. Using the rate of liquid hydrogen boiloff, the amount of additional hydrogen needed for a 14-day mission could be estimated. The thermal conductivities used in the heat transfer analyses are listed in table II along with material densities for each type of insulation. These property values were obtained from L. Capadona (2005, NASA Glenn Research Center, Cleveland, OH, personal communication) and references 5 to 7.

calculations, the vacuum jacket weight was also added to the total. The vacuum jacket weight was estimated assuming an aluminum jacket with a thickness of 0.138 in.

The results of the weight calculations are shown in figure 1, where the combined weight for each insulation approach is plotted as a function of insulation or vacuum gap thickness. The vacuum-jacketed approach with and without a MLI blanket provide the lightest thermal insulation design solution. The heaviest approach is the high-density, high-strength aerogel with no vacuum.

The difference in weight between the vacuum-jacketed approaches and the other designs is primarily due to the difference in the amount of additional propellant needed to account for boiloff, which is a direct result of the superior thermal insulation performance of the vacuum-jacketed approaches. This is illustrated in figures 2 and 3, where the total weight curves are decomposed into two curves: a curve representing the boiloff contribution and a curve representing the sum of all other weight contributors such as the tank, propellant, insulation, and vacuum jacket weights. Figure 2 shows the weight contributions for the vacuum jacket design with a MLI blanket, and figure 3 shows the weight contributions for the low-density aerogel under a vacuum. The amount of boiloff for the low-density aerogel is more than 10 times the amount needed for the vacuum-jacketed design.

TABLE. II.—INSULATION DENSITIES AND THERMAL CONDUCTIVITIES USED IN THERMAL ANALYSES TO ASSESS THERMAL INSULATION SCHEMES

Insulation approach	Density, lb/ft^3	Thermal conductivity, Btu/ft·hr·°F
High-density aerogel (no vacuum)	28.094[a]	0.0202[a]
High-density aerogel (vacuum)	28.094[a]	0.0101[b]
Low-density aerogel (no vacuum)	6.237[c]	0.0092[c]
Low-density aerogel (vacuum)	6.237[c]	0.0046[b]
Airex[d] spray-on foam insulation	3.900[e]	0.0140[e]
Vacuum jacket with multilayer insulation	1.500[f]	0.0002[f]

[a]From L. Capadona, 2005, NASA Glenn Research Center, Cleveland, OH, personal communication.
[b]Estimated as one-half the "no vacuum" conductivity value.
[c]From reference 5.
[d]Alcan Airex AG, Sins, Switzerland.
[e]From reference 6.
[f]From reference 7.

The combined weight of the tank system was calculated for each candidate insulation scheme and insulation thickness by summing the weights of the tank structure, the insulation, the propellant, and the additional propellant needed to account for the boiloff. For all weight calculations, a tank mass of 130 lb (65 lb per tank) was assumed. For the vacuum-jacketed weight
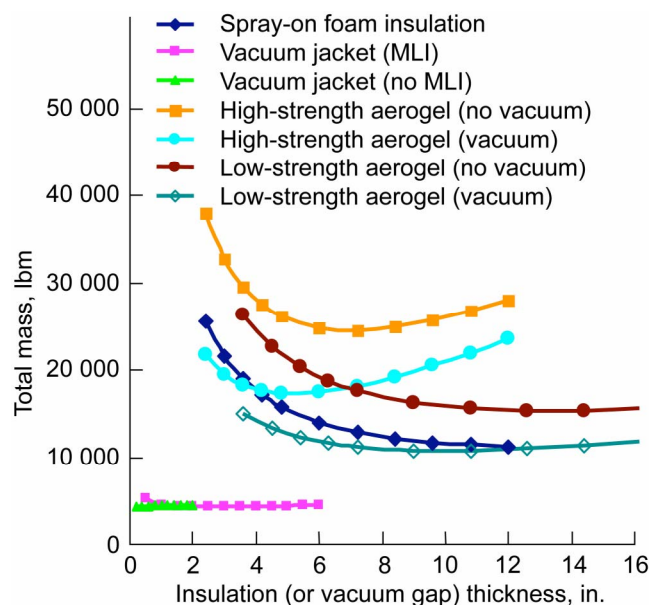

Figure 1.—Combined weight estimates for tank, propellant (including boiloff), and insulation for 14-day mission plotted versus insulation thickness for various insulating schemes (–70 °F ambient temperature). MLI refers to multilayer insulation blanket.
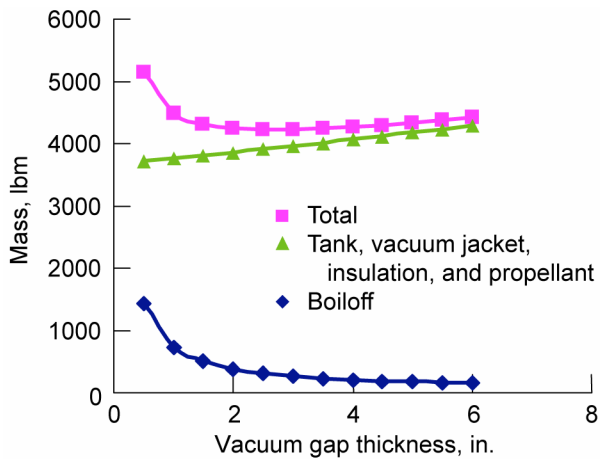
Figure 2.—Contribution from tank structure, insulation, propellant, and boiloff to total mass for vacuum-jacketed tank with MLI blanket for 14-day mission (–70 °F ambient air temperature).
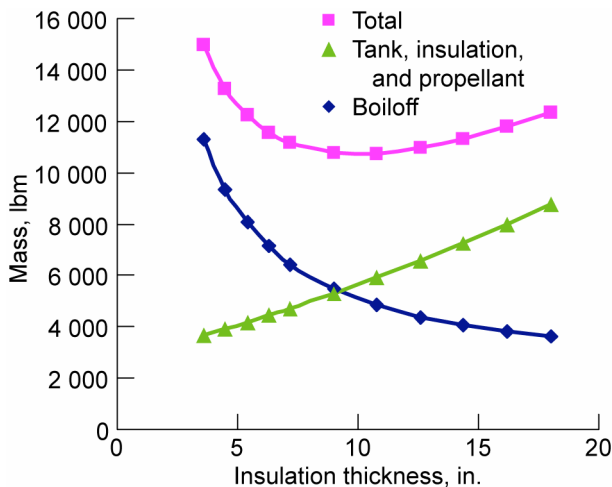

Figure 3.—Contribution from tank structure, insulation, propellant, and boiloff to total mass for low-strength aerogel insulation under vacuum for 14-day mission (–70 °F ambient air temperature).

The results shown in figures 1 through 3 illustrate the fact that neither SOFI insulation nor the high- and low-strength aerogel insulation approaches are viable design solutions for cryogenic hydrogen storage for a 14-day mission. For instance, figure 3 indicates that in order to provide 2645 lb of propellant to the power system over a 14-day mission using the low-density aerogel approach (the most efficient approach aside from the vacuum jacket design) with 10 in. of insulation, one would need to carry 5000 lb of additional propellant to account for boiloff. This is obviously not a viable design solution. The vacuum-jacketed approach is the only viable design approach for a 14-day mission.

It should be noted that for missions of shorter duration, the use of aerogels begin to rival the vacuum-jacketed design, since for shorter duration missions the boiloff mass becomes
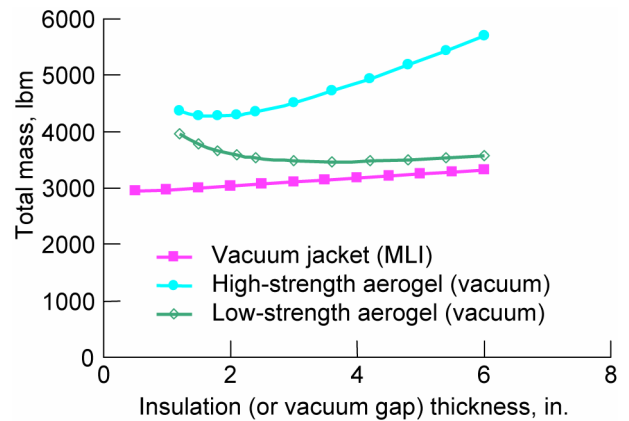

Figure 4.—Combined weight estimates for tank, propellant (including boiloff), and insulation for 5-hr mission versus insulation thickness for various insulating schemes (–70 °F ambient temperature).

less significant. This is illustrated in figure 4, where the combined tank system weights are plotted versus insulation thickness for a 5-hr mission.

Analysis of a Vacuum-Jacketed Design: Comparison of Aluminum and Graphite/Epoxy Composite Inner Tank Designs

This section reports on a series of thermal and structural analyses that were performed on the vacuum-jacketed tank design in order to determine the minimum required tank thicknesses (and minimum tank weights) to ensure structural integrity of the tank under the expected operational loads. These analyses were performed on both aluminum and graphite/epoxy composite designs subjected to tank pressurization loads, vehicle acceleration loads, and the steady-state thermal loads expected at altitude. This section focuses on the inner tank design. Weight estimates for the outer tank in a vacuum-jacketed design will be examined in the next section.

Aluminum Tank Design

The aluminum vacuum-jacketed design is illustrated in figure 5. The tank design consists of two thin metal tanks separated by a vacuum gap. The outer tank provides the vacuum jacket and carries external atmospheric pressure. The inner tank contains the cryogenic hydrogen under the operating internal pressure. The design also makes use of a central rod support which passes through the center of the tanks, protruding through the tanks at the top and bottom poles. The central rod support provides structural rigidity to the inner tank, a port for filling and draining propellant, and a means of mounting the tank to the vehicle. The central rod
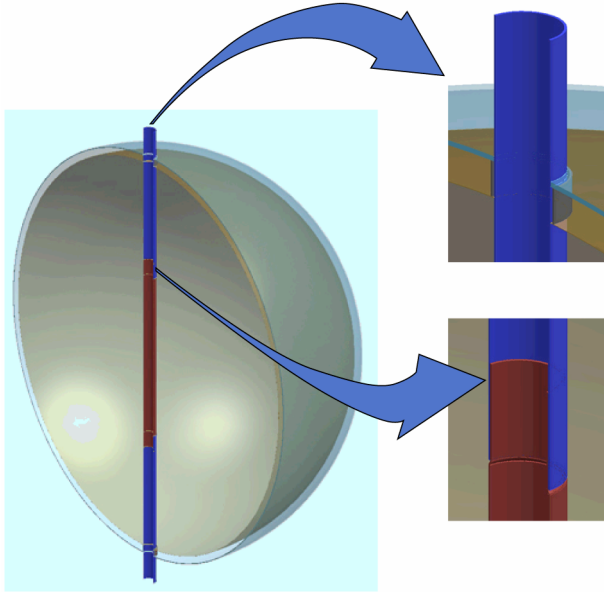
Figure 5.—Aluminum vacuum-jacketed tank design.

analysis. The thermal solution was performed using the P/Thermal module available in MSC.Patran (MSC.Software Corporation, Santa Ana, CA). Both convection and radiation boundary conditions were imposed. The boundary conditions imposed to each surface are summarized in table III. The outer surface of the support rod outside the outer tank envelop was assumed adiabatic, as it was assumed that this surface would be insulated to limit the heat penetration. Heat flow across the vacuum gap and MLI blanket was simulated by using an effective thermal conductivity; a value of 9.24×10^{-5} Btu/ft·hr·°F was assumed. The thermal conductivity of 2014–T6 aluminum, used in this analysis, is given in table IV. The results of the thermal analysis solution are illustrated in figure 6, where the steady-state temperature contours in the tank structure are plotted.

support is approximately 10 ft long, so that the rod extends from both poles approximately 9 in., allowing enough length for mounting hardware to attach the tank to the vehicle structure. It was assumed to have a 4-in. diameter. The inner tank is welded to the central rod support at both the top and bottom poles. Also, the inner and outer tanks are connected to one another at the top and bottom poles using connecting rings (zoomed view in fig. 5). At each pole, the connecting ring is welded to the inner and outer tanks, and this maintains the vacuum gap thickness at the poles and provides the vacuum seal between the tanks. In the current assessment, the tanks, support rod, and connecting rings are sized, and weights are estimated assuming that all components are fabricated from 2014–T6 aluminum. The design also makes use of a rod slip joint near the center of the support rod to accommodate thermal contraction of the tank structure at cryogenic temperatures.

The design described above uses the connecting rings to maintain the vacuum between the inner and outer tanks. An alternative approach, however, may be employed such as the use of baffles between the tanks to maintain the vacuum and allow for differential thermal expansion between the inner and outer tanks. In addition, it may be necessary to use some sort of standoff, possibly in the form of springs or struts, near the equator of the tank, to prevent contact between the two tanks. A design that utilizes baffles or standoffs is not considered in the current tank weight assessments.

A thermal analysis of the vacuum-jacketed tank design (with MLI) was performed to obtain the steady-state temperature profiles in the tank at altitude. These were used as the thermal loads and temperature conditions for the structural

TABLE III.—CONVECTION AND RADIATION BOUNDARY CONDITIONS USED IN THERMAL ANALYSIS OF ALUMINUM 2014–T6 VACUUM-JACKETED TANK

Surface	Convection coefficient, h_{conv}, Btu/ft^2·hr·°F	Ambient temperature, T_∞, °F	Emissivity, ε
Inner surface inner tank (below fill line)	1.76	–423	0.0
Inner surface inner tank (above fill line)	0.88	–418	0.0
Outer surface outer tank	0.176	–70	0.02
Outer surface support rod (inside tank, below fill line)	1.76	–423	0.0
Outer surface support rod (inside tank, above fill line)	0.88	–418	0.0

TABLE IV.—MATERIAL PROPERTIES OF 2014–T6 ALUMINUM USED FOR THERMAL AND STRUCTURAL ANALYSIS OF VACUUM-JACKETED ALUMINUM TANK

Density, lb/in^3 .... 0.101
Young's modulus, Msi 10.5
Poisson's ratio 0.33
Coefficient of thermal expansion, /°F .... 1.3×10^{-5}
Thermal conductivity, Btu/ft·hr·°F 88.98
Specific heat, Btu/lb·hr °F 0.21
Tensile yield strength, ksi 60
Tensile ultimate strength, ksi 70
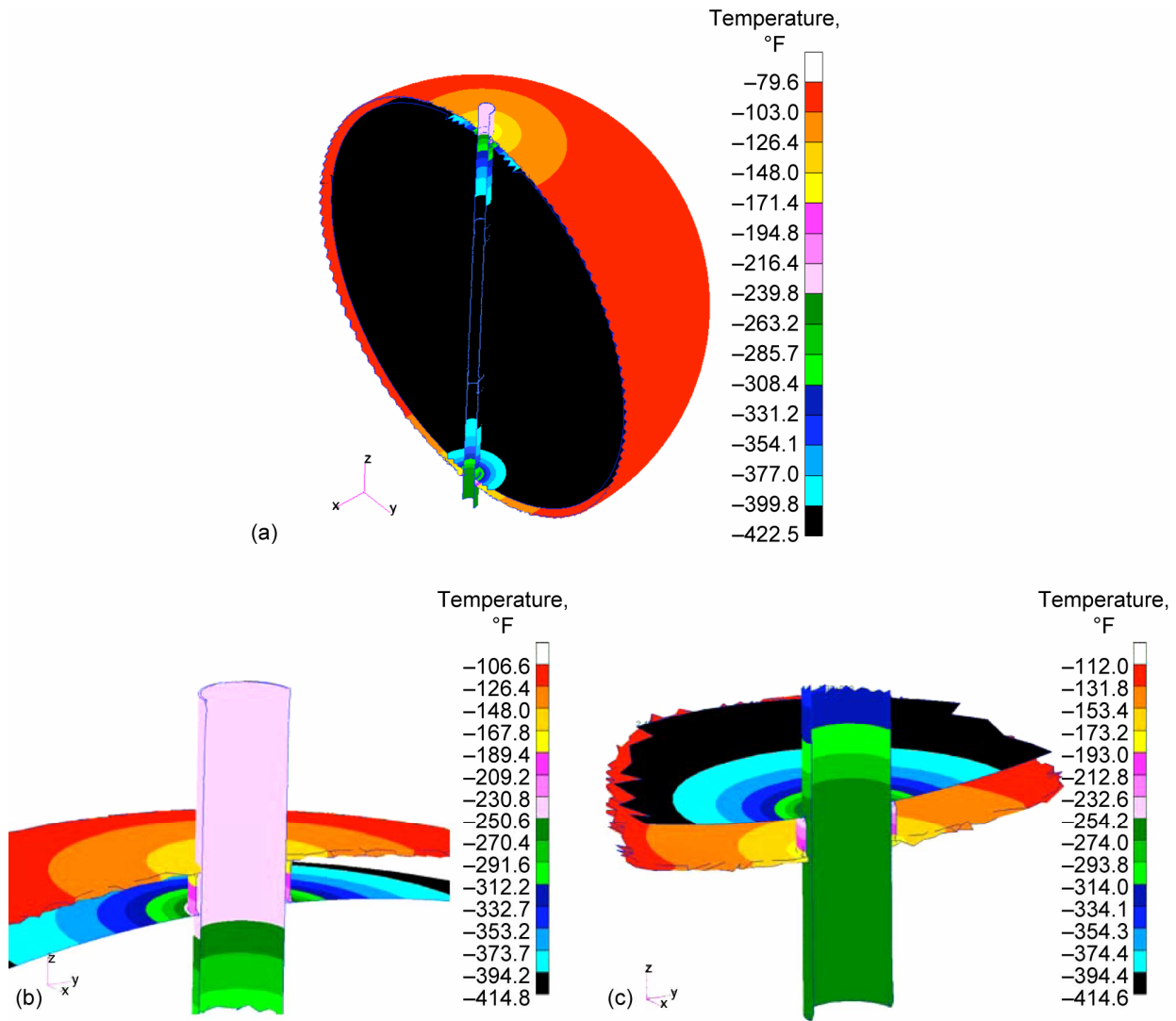
Figure 6.—Temperature contour plots in aluminum vacuum-jacketed (with MLI) tank design for steady-state conditions at altitude. (a) Global view. (b) Top rod-tank junction. (c) Bottom rod-tank junction.

The structural analysis of the aluminum vacuum-jacketed tank was performed using MSC.Nastran (ref. 8) to predict the structural response of the tank under vehicle operating conditions at altitude. The loads applied to the tank structure include a 30-psi internal pressure, a uniform external pressure on the outer tank of 0.8 psi, a 3.5g vertical acceleration load, and a 0.5g lateral acceleration load, along with the thermal loads determined with the thermal analysis solution. The structural analysis solution was performed for two sets of load combinations: a solution where only the pressure and acceleration loads were applied and a solution where the pressure, acceleration, and the thermal loads were applied. The 30-psi internal pressure and the lateral and vertical acceleration loads were applied to the tank structure using an asymmetrical internal pressure, which is statically equivalent to the combination of the internal pressure and the acceleration loads. The finite element model of the tank was constrained by constraining a row of nodes at the top and bottom ends of the support rod. At the top end of the support rod, the nodes were constrained against rotation and all three translational degrees of freedom. At the bottom end of the support rod, the nodes were constrained against rotation and the two lateral translational degrees of freedom. The material property values for 2014–T6 aluminum used in the structural analysis solution are listed in table IV.

The structural analysis was initially performed assuming an inner tank and support rod thickness of 0.03 in. This value was chosen as a starting thickness, as it was believed that 0.03 in. was the minimum achievable tank thickness, given the diameter of the tank. The initial analysis solution yielded negative margins of safety. As such, the support rod thickness was increased and the analysis was repeated. This process was repeated until the analysis resulted in positive margins of safety for the inner tank, the support rod, and the connecting rings.

The final results of the structural analysis solution are illustrated in figure 7 and table V. In figure 7, the predicted maximum principal stress contours for the two analysis solutions (with and without thermal loads) are plotted. The location of the maximum principal stress in the tank is in the pole region at the junction of the tank and support tube. Table V is a summary of the maximum principal stress and the minimum margin of safety for each tank component, for the two analysis solutions. Margins of safety are calculated for both ultimate load and yielding, using the appropriate factors of safety. In view of the results shown in figure 7 and table V, it appears that the application of the pressure and acceleration loads result in much higher principal stresses than the application of the thermal loads alone.

TABLE V.—METAL VACUUM-JACKETED TANK
DESIGN STRUCTURAL ANALYSIS RESULTS

	Load case	Predicted maximum principal stress, psi	Margin of safety on ultimate strength[a]	Margin of safety on yield strength[b]
Inner tank	Pressure and acceleration	35 000	0.333	0.558
	Pressure, acceleration, and temperature	38 900	0.200	0.402
Support rod and rings	Pressure and acceleration	31 400	0.486	0.737
	Pressure, acceleration, and temperature	41 900	0.114	0.302

[a]Factor of safety is 1.5.
[b]Factor of safety is 1.1.

Table VI lists the minimum thicknesses required to have positive margins of safety under tank operational loads, including the steady-state thermal loads. From the required tank thicknesses, the tank component weights were determined. The combined weight of the inner tank, support rod, and connecting rings is 128 lb.

TABLE VI.—WEIGHT ESTIMATES FOR ALUMINUM
INNER TANK DESIGN

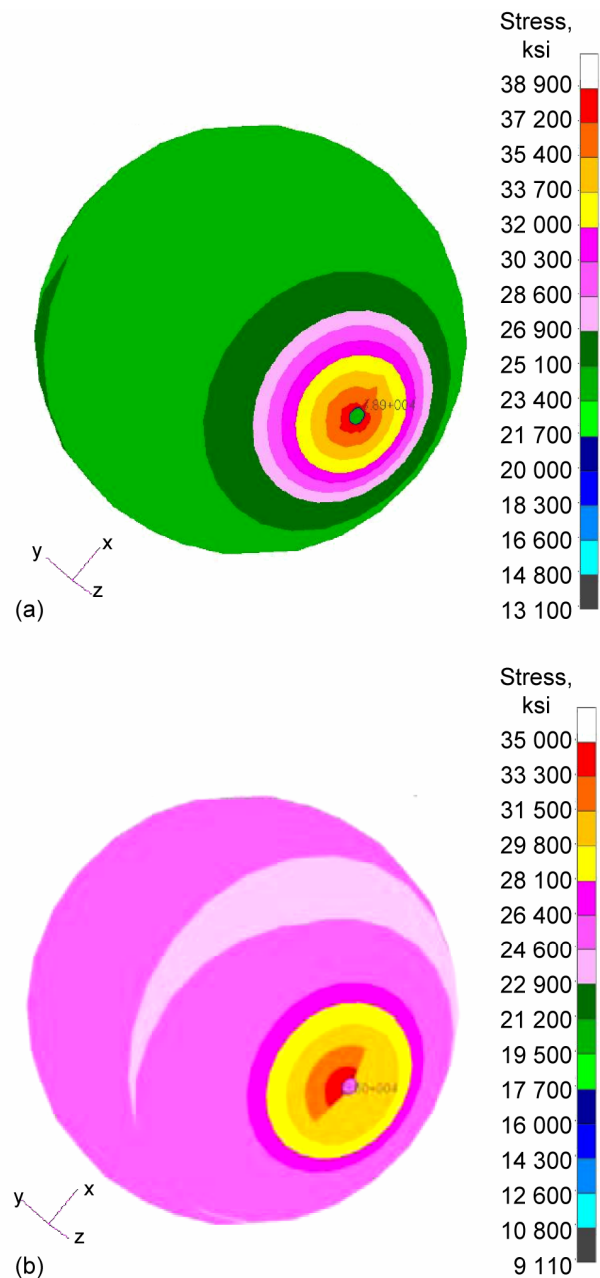|	Outer diameter, in.	Thickness, in.	Volume, in³	Mass, lbm
Inner tank	102.38	0.031	1006.00	102
Support rod (120.34 in. length)	4.00	0.170	246.20	25
Connecting rings (2 rings, each with 1.824 in. length)	4.35	0.170	8.15	1
Total	---------	---------	---------	128

Figure 7.—Predicted maximum principal stress contours in aluminum inner tank. (a) Results for pressure, acceleration, and temperature loads. (b) Results for pressure and acceleration loads.

Composite Inner Tank

This section reports on the structural analysis of a graphite/epoxy inner tank in a vacuum-jacketed design application. The graphite/epoxy inner tank design consists of the spherical tank and two support tubes, one at the top and bottom poles. The support tubes provide a port for filling and draining propellant and a means of mounting the tank to the vehicle. It is expected that the support tubes and spherical tank will be co-cure processed to obtain a rigid connection between the tank and tubes. To be consistent with the aluminum tank design, the outer diameter of the support tubes was 4 in. They were assumed to be 12 in. long. Unlike the assessment of the aluminum inner tank design, this analysis did not include an outer tank or connecting rings. In this analysis, it was assumed that the vacuum-jacketed tank assembly could be constructed such that the inner tank would be isolated both thermally and structurally from the outer tank. This could be achieved with the use of baffles between the support tubes and outer tank to maintain the vacuum between the tanks and allow the inner and outer tanks to act independently in the structural sense. Also, the use of an insulator ring in concert with the baffles, along with the vacuum space between the tanks, would thermally isolate the inner and outer tanks.

Again, both thermal and structural analyses were performed. The thermal analysis was performed to obtain the steady-state temperature profiles in the tank at altitude. These were used as the thermal loads and temperature conditions for the structural analysis. Both analyses were performed with ABAQUS (ref. 9), using the finite element model shown in figure 8. The model of the inner tank and support tubes consists of 13 440 C3D8 and C3D6 elements (fig. 8(a)). Also, the liquid hydrogen was modeled explicitly using 21 056 C3D8 and C3D6 elements. These are shown as green elements in figure 8(b).

The graphite/epoxy composite material properties used in the analyses were calculated from the fiber and matrix constituent property values and the Integrated Composite Analyzer (ICAN) code (ref. 10). ICAN is based on a combination of composite micromechanics and lamination theory. IM7 carbon fibers (Hexcel Corporation, Stamford, CT) and 977–2 epoxy resin (Cytec Engineered Materials, Inc., Tempe, AZ) were assumed. The constituent property values are listed in table VII. Resin properties were estimated based on typical 977–2 epoxy properties, modified to account for the expected effect of the nanoclay platelets (S. Miller, 2005, NASA Glenn Research Center, Cleveland, OH, personal communication). The fiber and matrix constituent properties were available at room temperature (70 °F). Some limited properties were available on the epoxy resin at –423 °F. The IM7 carbon fiber properties were assumed to remain constant with variations in temperature. A laminate layup of $[0/\pm15/\pm30/\pm45/\pm60/\pm75/90]_s$ was assumed, as this layup yields a quasi-isotropic laminate, a likely choice for a pressurized spherical shell structure. Since the constituent properties were only available at room temperature (70 °F)

and at –423 °F, the composite laminate properties were determined for these two temperatures. The composite laminate properties predicted by ICAN are listed in table VIII.
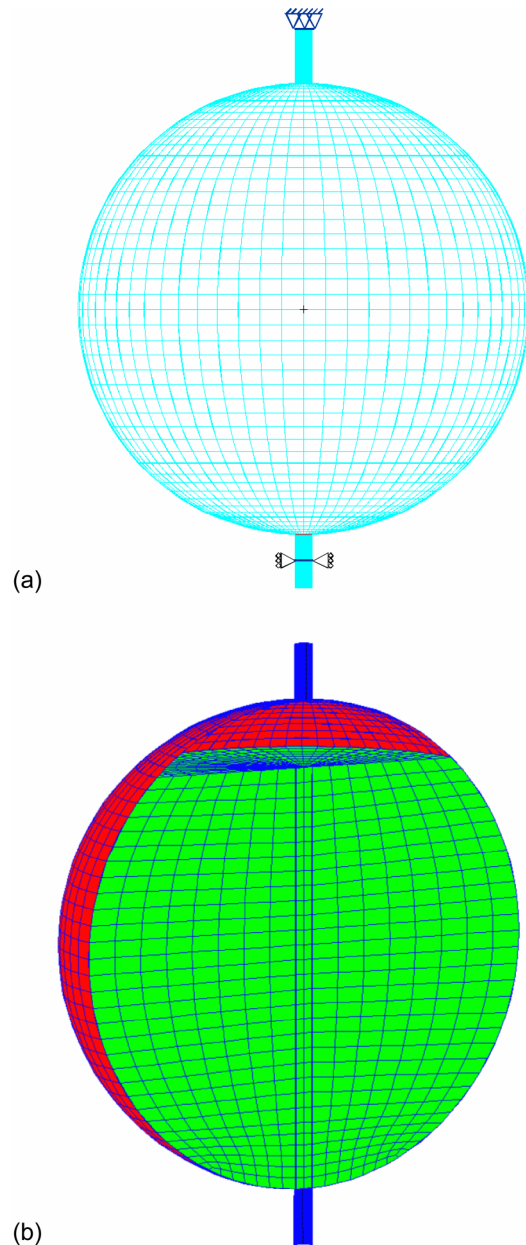

(a)

(b)

Figure 8.—Finite element mesh of graphite/epoxy inner tank. (a) Full mesh with supports. (b) Cutaway view showing LH$_2$ elements.

TABLE VII.—GRAPHITE/EPOXY CONSTITUENT PROPERTIES
USED TO CALCULATE COMPOSITE PROPERTIES

Constituent	Property	Temperature	
		–423 °F	70 °F
IM7 fiber[a]	Density, lb/in^3	0.07	0.07
	Longitudinal modulus, Msi	38.0	38.0
	Transverse modulus, Msi	2.8	2.8
	In-plane shear modulus, Msi	4.0	4.0
	Transverse shear modulus, Msi	4.0	4.0
	Longitudinal coefficient of thermal expansion, /°F	-0.5×10^{-6}	-0.5×10^{-6}
	Transverse coefficient of thermal expansion, /°F	4.0×10^{-6}	4.0×10^{-6}
	Longitudinal conductivity, Btu/in·hr·°F	4.0	4.0
	Transverse conductivity, Btu/in·hr·°F	.4	.4
	Specific heat, Btu/lb·°F	.17	.17
Nanoclay-enhanced epoxy	Density, lb/in^3	0.042	0.042
	Young's modulus, Msi	.9	.6
	Shear modulus, Msi	.31	.2
	Coefficient of thermal expansion, /°F	15.0×10^{-6}	35.6×10^{-6}
	Thermal conductivity, Btu/in·hr·°F	8.6×10^{-3}	9.0×10^{-3}
	Specific heat, Btu/lb·°F	.25	.25

[a]Hexcel Corporation, Stamford, CT.

TABLE VIII.—MATERIAL PROPERTIES FOR NANOCLAY-ENHANCED GRAPHITE/EPOXY
LAMINATE USED IN THERMAL AND STRUCTURAL ANALYSIS OF
COMPOSITE INNER TANK[a]

Property	Temperature	
	–423 °F	70 °F
Density, lb/in^3	0.059	0.059
Young's modulus, Msi In-plane Through-thickness	9.25 2.52	8.84 2.07
Shear modulus, Msi In-plane Interlaminar	3.56 .9	3.37 .63
Coefficient of thermal expansion, /°F In-plane Through-thickness	0.6×10^{-6} 8.8×10^{-6}	1.2×10^{-6} 16.8×10^{-6}
Thermal conductivity, Btu/in·hr·°F In-plane Through-thickness	1.22 .03	1.22 .03
Specific heat, Btu/lb·°F	0.193	0.193

[a]Properties calculated using ICAN and constituent property values from table VII.

TABLE IX.—CONVECTION BOUNDARY CONDITIONS USED IN THERMAL ANALYSIS OF
GRAPHITE/EPOXY INNER TANK

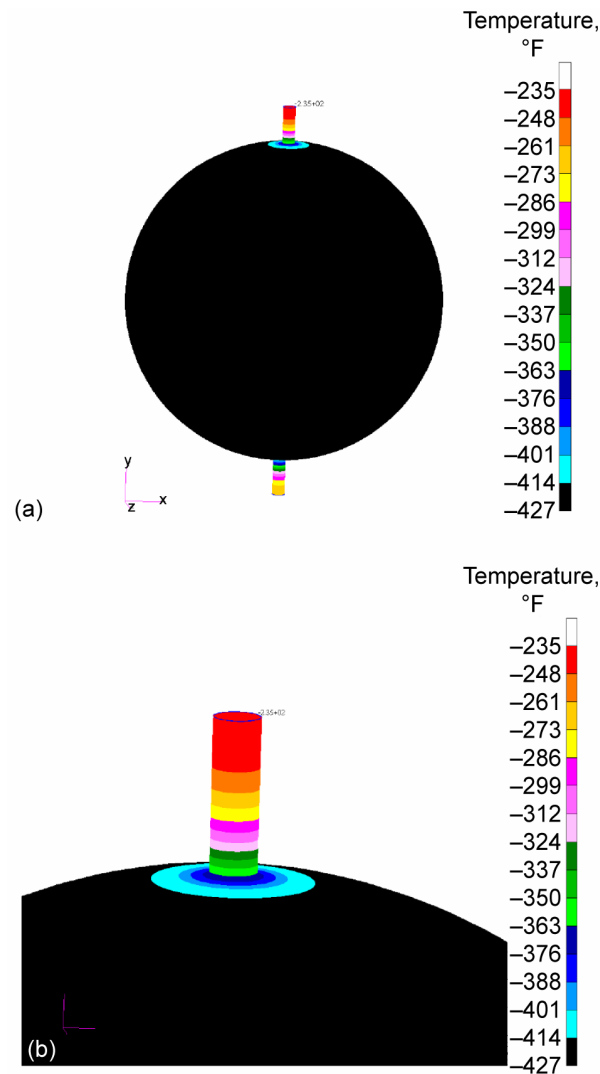| Surface	Convection coefficient, h_{conv}, Btu/ft^2·hr·°F	Ambient temperature, T_∞, °F
Inner surface inner tank (below fill line)	1.76	−423
Inner surface inner tank (above fill line)	0.88	−423
Outer surface support tubes (outside outer tank)	0.176	−70

Figure 9.—Temperature contour plots in graphite/epoxy inner tank and support tubes for steady-state conditions at altitude. (a) Global view. (b) Tank-tube interface.

The boundary conditions used for the thermal analysis of the graphite/epoxy inner tank are listed in table IX. Contrary to the assumption used in the thermal analysis of the aluminum inner tank, the outer surface of the support tubes outside the outer tank envelop was not assumed to be insulated. It was assumed that this surface would be exposed to the ambient air at a temperature of –70 °F. Also, radiation was not included. The results of the thermal analysis solution are shown in figure 9, where the steady-state temperature contours are plotted.

For the structural analysis solution, the model was constrained at the top and bottom support tubes (fig. 8(a)). At the top support tube, the top row of nodes was constrained against translation in all three directions. At the bottom support tube, a row of nodes at the midlength of the tube were constrained against lateral translation.

In order to determine the required minimum tank wall thickness, the structural analysis of the inner tank was performed for a variety of different wall thicknesses. The thickness of the support tubes was held constant at 0.1 in. These structural analyses were also performed for two sets of load combinations: a solution where only the internal pressure load (30 psi) and acceleration loads (3.5g vertical and 0.5g lateral) were applied and a solution where the pressure, acceleration, and the thermal loads were applied. Table X lists

the maximum predicted in-plane composite laminate stresses in the tank and support tubes for inner tank wall thicknesses of 0.08, 0.05, and 0.04 in. For the tank, the maximum hoop (σ_θ) and meridional (σ_ϕ) stresses are listed, whereas for the support tubes, the hoop and axial stresses are listed. The results are shown for the load combinations with and without the thermal loading. Using ICAN, the maximum fiber and matrix stresses were calculated from the composite laminate stresses. Margins of safety were calculated on the fiber and the matrix stresses using factors of safety 1.5 and 2.0. Negative margins of safety are highlighted in bold type.

Again, the maximum stresses in the tank occur near the poles at the junction of the tank and support tube. This is illustrated in figure 10, where the in-plane composite-level stress contours are plotted. The results are plotted for an inner tank wall thickness of 0.05 in., with and without the thermal loads.

Looking at the results in table X, it can be concluded that a tank wall thickness of 0.06 in. would result in positive margins of safety (based on a factor of safety of 2.0) on both the fiber and matrix stresses in the support tubes and the tank wall. Table XI lists the weight of the tank and support tubes for a tank with a wall thickness of 0.06 in. The combined weight of the support tubes and tank is approximately 118 lb.

TABLE X.—GRAPHITE/EPOXY INNER TANK STRUCTURAL ANALYSIS RESULTS

(a) Maximum stress in tank

	Inner tank thickness, in.	Composite stress, ksi		Fiber stress, ksi	Fiber margin[a]		Matrix stress, ksi	Matrix margin[b]	
		Hoop	Meridional		Factor of safety			Factor of safety	
					1.5	2.0		1.5	2.0
Pressure and acceleration loads	0.08	17.8	26.5	90.6	1.10	0.55	7.1	0.41	0.06
	.05	26.6	39.6	132.8	.40	.05	8.5	.18	**−.12**
	.04	33.5	51.5	173.4	.08	**−.2**	11.0	**−.10**	**−.32**
Pressure, acceleration, and thermal loads	0.08	17.1	25.4	85.6	1.20	0.64	6.4	0.56	0.17
	.05	26.4	39.8	133.9	.40	.05	8.5	.16	**−.13**
	.04	32.5	49.5	166.3	.12	**−.16**	10.6	**−.06**	**−.29**

(b) Maximum stress in support tubes

	Inner tank thickness, in.	Composite stress, ksi		Fiber stress, ksi	Fiber margin[a]		Matrix stress, ksi	Matrix margin[b]	
		Hoop	Axial		Factor of safety			Factor of safety	
					1.5	2.0		1.5	2.0
Pressure and acceleration loads	0.08	12.9	4.4	48.9	2.80	1.90	2.8	2.60	1.70
	.05	15.1	4.2	58.5	2.20	1.40	3.2	2.10	1.30
	.04	17.8	4.3	68.4	1.73	1.05	3.8	1.63	.97
Pressure, acceleration, and thermal loads	0.08	12.3	4.4	48.6	2.84	1.90	2.63	2.80	1.85
	.05	15.2	4.2	59.9	2.10	1.30	3.3	2.10	1.30
	.04	17.0	4.3	66.7	1.80	1.10	3.63	1.75	1.10

[a]Based on assumed fiber strength of 280 ksi.

[b]Based on assumed matrix strength of 15 ksi.

TABLE XI.— WEIGHT ESTIMATES FOR GRAPHITE/EPOXY
INNER TANK DESIGN

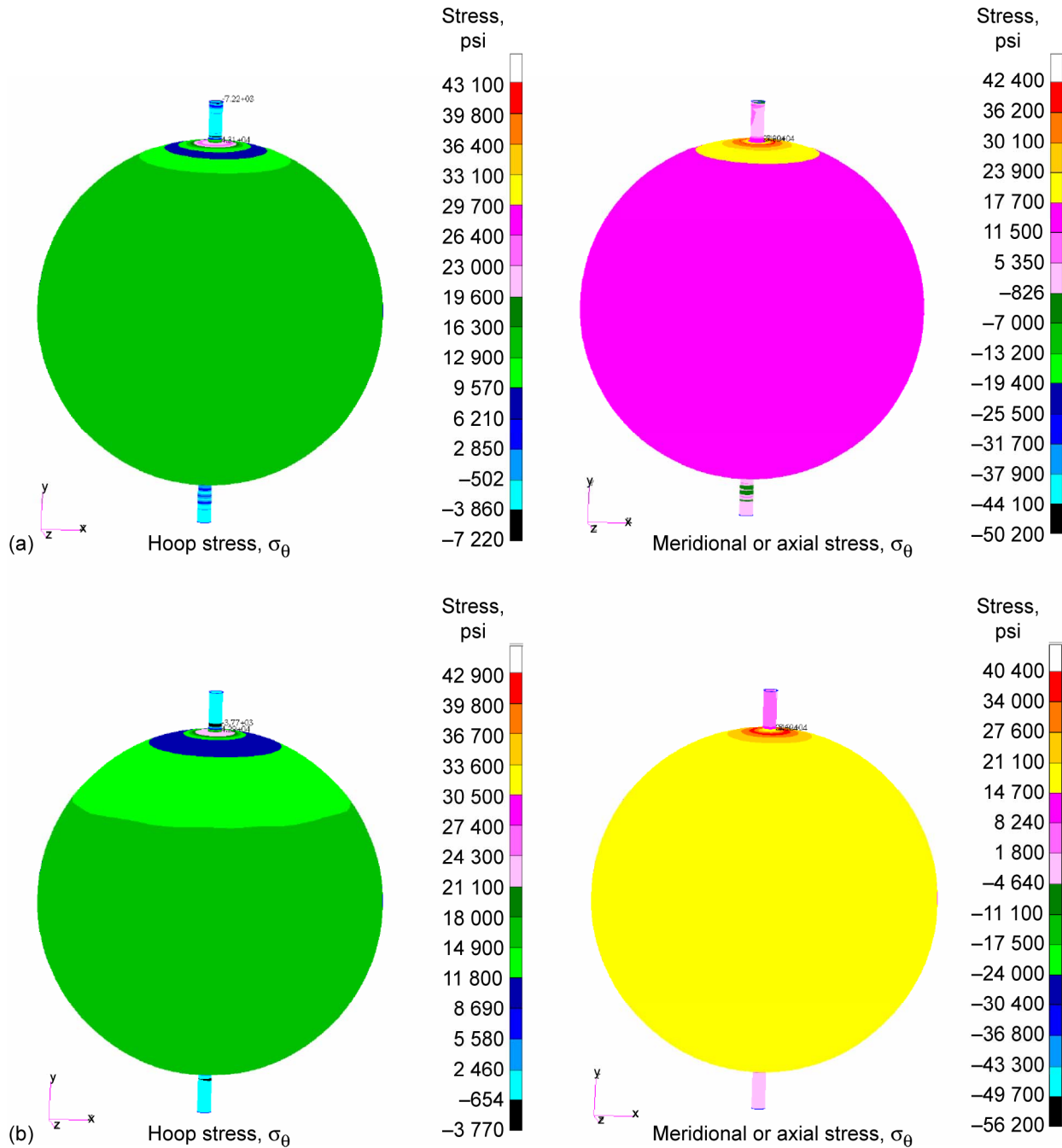|	Outer diameter, in.	Thickness, in.	Volume, in^3	Mass, lbm
Inner tank	102.48	0.06	1977.29	116.66
Two support tubes (12-in. length)	4.0	0.1	29.4	1.73
Total	--	--	--	118.39

Figure 10.—Predicted in-plane composite-level stresses in graphite/epoxy inner tank for a tank wall thickness of 0.05 in.
(a) Results for pressure, acceleration, and temperature loads. (b) Results for pressure and acceleration loads only.

Buckling Analysis of Outer Tank: Comparison of Metal and Composite Outer Tank Designs

The purpose of this section is to provide preliminary weight estimates of the outer tank in a vacuum-jacketed tank design. The outer tank is sized against buckling failure under the 1-atm external pressure load. Four materials are considered: the aluminum-lithium alloy LiAl 2090, the aluminum alloy Al 2014–T6, the stainless steel CRES 304L, and a $[0°/\pm 45°/90°]_s$ IM7 graphite/977–2 epoxy laminate. Also, both uniform-thickness (i.e., unstiffened) and grid-stiffened structural concepts were considered.

The analysis and sizing of the outer tank was accomplished using the MSC/NASTRAN finite element analysis package along with the HyperSizer (Collier Research Corp., Hampton, VA) stiffened structural optimization software. The HyperSizer software links with NASTRAN finite element models, extracting loads that can then be used to size a section of the structure, including the effects of stiffeners. If needed, HyperSizer can then update the NASTRAN model with new properties based on the results of the section sizings.

The MSC/NASTRAN finite element model used for this analysis is illustrated in figure 11. An inner and outer tank were each modeled using 3200 shell elements (CQUAD4). The model also includes beam elements that represent a central support rod and an internal stringer support system, which support the inside of the inner tank. Short beam elements were also used to connect the inner and outer tank shells to a node on the central support rod at the top and bottom poles. The shell arrangements representing the inner and outer tanks are open at both poles. The short beam elements tie the free edge of the tank shell elements to the pole node. A total of 884 CBAR elements were used to simulate the central support rod and inner tank stringer supports and to tie the tank shells to the central support rod at the pole nodes. The model is constrained at the pole nodes. The top pole node is fixed against all three translational degrees of freedom and all three rotational degrees of freedom. At the bottom pole, the pole node is constrained against translational motion in the x- and y-directions (free vertical translation) and all three rotational degrees of freedom are possible. This model was originally constructed to perform preliminary design analyses of the vacuum-jacketed design approach under a variety of loading conditions. It was decided that this same model would be useful for the purpose of sizing the outer tank (and estimating weight) against buckling failure.

In order to perform separate structural design optimizations for each region of the structure based on the local loads in each region, the structure must be separated into different sections. These sections, which HyperSizer refers to as "components," are defined in MSC/NASTRAN during the model definition. Structural analysis results from the MSC/NASTRAN finite element model are extracted by HyperSizer for each component and each component is sized
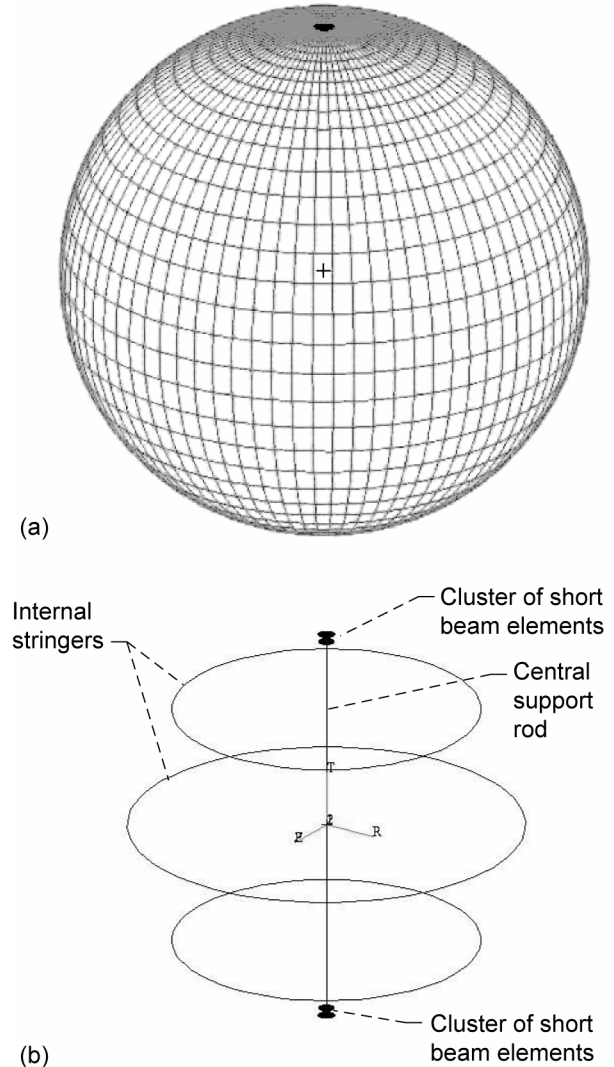

(a)

(b)

Figure 11.—Finite element mesh of outer tank, including tank wall and interior beams. (a) Tank. (b) Interior beam arrangement.

independently according to its local loads. The total weight is then the sum of the weights for each component in the structure.

For the outer tank analysis, the components are illustrated in figure 12. Since the current analysis is only a preliminary assessment and since a detailed design of the tank in the pole regions (and vehicle attachment points at the poles) is not yet fully determined, the local loads calculated by MSC/NASTRAN in the components near the poles are inconsequential. As a result, the preliminary sizing of the outer tank was performed based solely on a component near the tank equator. This component is identified in figure 12. Thus, the estimated minimum tank weight for each material and design option reported here was calculated as the product of the minimum acceptable unit weight (weight per unit area, determined by HyperSizer for this equatorial component) times the total area of the outer tank.
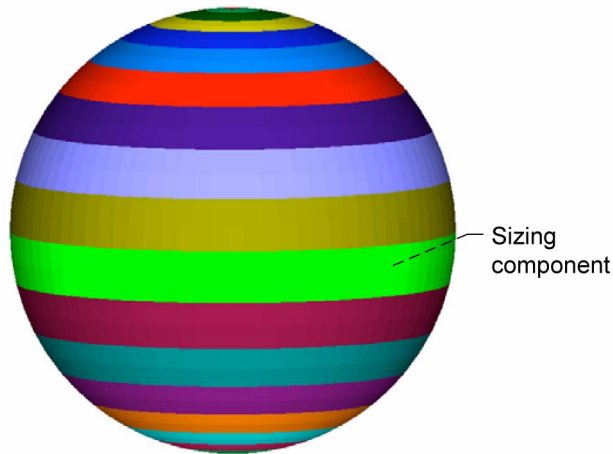
Figure 12.—Outer tank illustrating dissection of tank into different components. Noted is equatorial component used for preliminary sizing and tank weight estimate.

Within HyperSizer, the sizing of the component is accomplished by selecting the desired structural concepts and materials to be considered and specifying desired limit and ultimate factors of safety. In addition, for curved panel buckling analysis, a buckling knockdown factor and buckling lengths must be specified. The buckling knockdown factor is employed to correlate theoretical (Raleigh-Ritz) curved panel buckling loads (which are typically very nonconservative) with experimental buckling loads. This is due to the fact that curved panel buckling is highly dependent on slight variations in thickness and flaws that occur randomly in structures. The necessary buckling knockdown factor is also a function of thickness, as the small variations and flaws become of greater importance as the structure becomes thinner (refs. 11 and 12). The buckling lengths characterize the controlling buckling mode shapes for the curved panel and are a function of the thickness and radius of curvature of the panel. These buckling lengths must be verified through an independent finite element analysis of the curved panel.

A selection of grid-stiffened structural concepts available in HyperSizer is shown in figure 13. For the outer tank sizing exercise, only the bi-grid and iso-grid designs were selected as potential candidates. It should be noted that HyperSizer admits a great deal of freedom in optimizing the grid-stiffened panels shown in figure 13. For instance, the iso-grid panel concept allows the grid stiffeners in each direction to be different materials and have different heights, thicknesses, and spacings. For the sizing performed in this section, many of these sizing variables were linked such that the entire panel was required to be the same material, while four independent geometric variables remained: facesheet thickness, stiffener thickness, stiffener height, and stiffener spacing. HyperSizer optimizes the panel by varying these geometric variables, each within a specified range, while also varying the materials and or concepts in order to determine the lightest weight configuration that satisfies all failure analysis checks.

Table XII provides the factors of safety, buckling lengths, and buckling knockdown factors employed in the sizing of the outer tank. The factors of safety are in accordance with U.S. Federal Aviation Administration Regulations (FAR, ref. 4). In HyperSizer, global buckling (such as panel buckling, crippling, and buckling-crippling interaction) is treated as an ultimate failure event and thus employs the ultimate load factor of 1.5. Local buckling, on the other hand, is a local failure event. After the onset of local buckling, the structure can typically support a great deal of additional load prior to collapse as stresses are redistributed (ref. 13). Local buckling of the facesheet and the grid stiffeners within HyperSizer thus employ the limit load factor of 1.0. The employed buckling lengths and knockdown factors are different for the stiffened and unstiffened configurations because they have different effective thicknesses. The employed values were obtained from independent panel-level finite element analyses (C.S. Collier, 2005, Collier Research and Development Corp., Hampton, VA, personal communication).
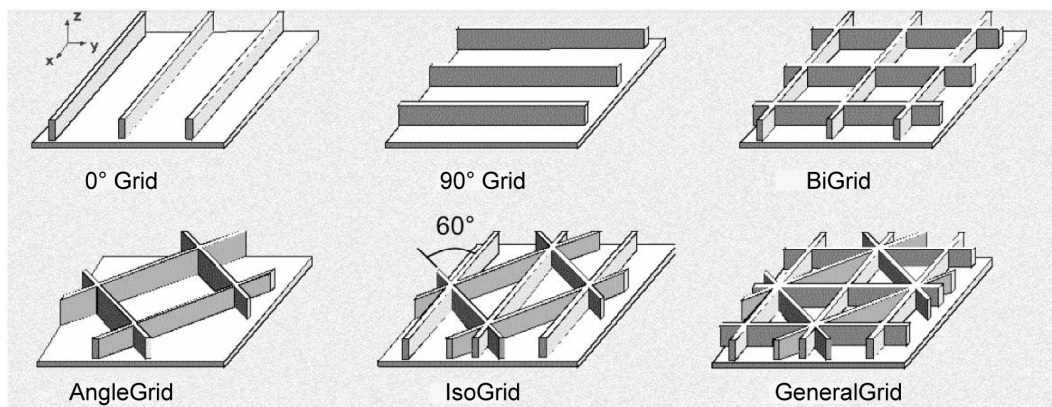

Figure 13.—Grid-stiffened panel concepts available in HyperSizer (Collier Research Corp., Hampton, VA) software.

TABLE XII.—FACTORS OF SAFETY AND BUCKLING PARAMETERS USED IN OUTER TANK BUCKLING ANALYSIS

Concept	Limit load factor (local buckling)	Ultimate load factor (global buckling, crippling)	Buckling lengths, in.	Buckling knockdown factor
Unstiffened	1.0	1.5	6×6	0.4
Grid stiffened	1.0	1.5	7×7	0.75

The material properties employed in the outer tank sizing are listed in table XIII. These are the property values listed in the HyperSizer database. The graphite/epoxy properties listed in table XIII are the ply-level properties for unidirectional plies of IM7 graphite/977–2 epoxy with a fiber volume fraction of 60 percent. The material properties used in the sizing analyses were calculated in HyperSizer using the ply properties and classical lamination theory equations, assuming an 8-ply $[0°/\pm45°/90°]_s$ laminate. It should also be noted that the allowables of the ply material listed in table XIII have been knocked down to account for matrix cracking, which must be avoided in pressure vessel applications.

A uniform, external pressure of 1 atm was applied to the outer surface of the outer tank, and the structural analysis of the tank was performed with MSC/NASTRAN. The results of this analysis are shown in figure 14, where the in-plane (membrane) force components are plotted. The forces in the elements appear to be nearly biaxial and uniform, with the exception of the regions near the poles. For the equatorial component (identified in fig. 12), the force resultants are N_θ = –387.5 lb/in., N_ϕ = –389.8 lb/in, and $N_{\theta\phi}$ = 0.03 lb/in. Further, for all regions of the tank with the exception of the poles, the N_θ and N_ϕ force resultants are between –385 and –390 lb/in.

TABLE XIII.—MATERIAL PROPERTIES USED IN OUTER TANK SIZING ANALYSIS

	LiAl 2090	Al 2014–T6	CRES 304L steel[a]	Graphite/epoxy IM7/977–2 ply[b]
Response property[c]				
Density, ρ, lb/in³	0.0975	0.11	0.286	0.057
Young's modulus				
E_1 tension, Msi	11.6	10	26	23.3
E_1 compression, Msi	11.6	10	26	21.5
E_2 tension, Msi	11.6	10	26	1.35
E_2 compression, Msi	11.6	10	26	1.35
Shear modulus, G_{12}, Msi	4.41	3.76	10.5	0.75
Poisson's ratio, ν_{12}	.315	.33	.238	.3
Stress allowables				
Ultimate strength				
σ_{11}^u tension, ksi	72.5	70	174	139.8
σ_{11}^u compression, ksi	72.5	70	174	129
σ_{22}^u tension, ksi	72.5	70	175	8.1
σ_{22}^u compression, ksi	72.5	70	175	8.1
Yield strength				
σ_{11}^y tension, ksi	68.2	60	137	139.8
σ_{11}^y compression, ksi	68.2	60	83	129
σ_{22}^y tension, ksi	68.2	60	125	8.1
σ_{22}^y compression, ksi	68.2	60	142	8.1
Ultimate shear strength				
τ_{12}^u, ksi	54	40.4	95	11.6

[a]CRES 304L properties in HyperSizer (Collier Research Corp., Hampton, VA) database are the same as AMS 5519 from Metallic Materials and Elements for Aerospace Vehicle Structures. MIL–HDBK–5J, 2003.
[b]IM7 graphite fibers (Hexcel Corporation, Stamford, CT) and 977–2 epoxy resin (Cytec Engineered Materials, Inc., Tempe, AZ).
[c]The 1-direction is in rolling direction for CRES 304L steel, and in direction of fibers for graphite/epoxy.
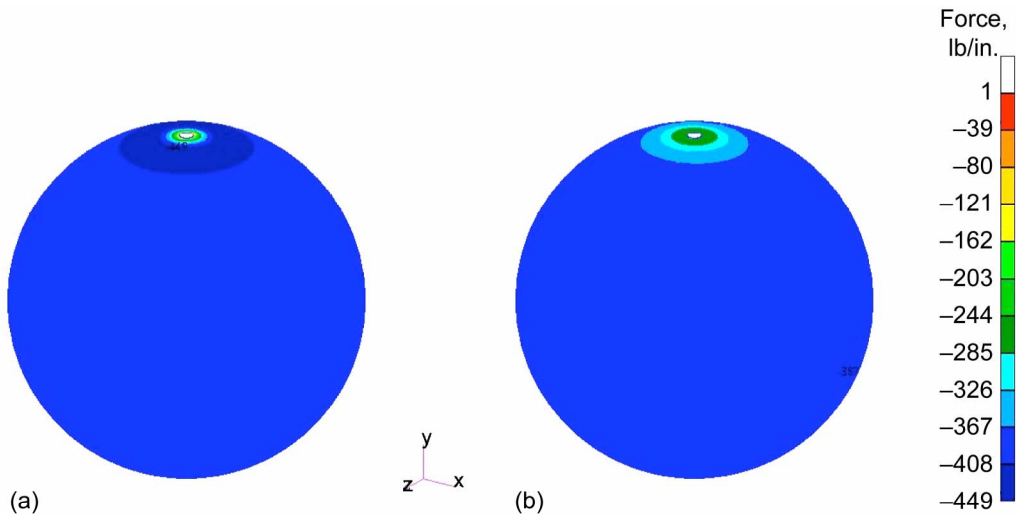
Figure 14.—Shell force contours in outer tank due to 1-atm uniform external pressure calculated in finite element solution. (a) N_θ force contour. (b) N_ϕ force contour.

Note that the analytical solution for a thin hollow sphere of radius r subjected to a uniform external pressure P yields the expression for the membrane forces:

$$N_\theta = N_\phi = -\frac{Pr}{2} \qquad (1)$$

Thus, for an outer tank radius of 53.21 in. and an exterior pressure of 14.7 psi, the analytical solution predicts a biaxial force resultant of –391 lb/in. throughout the tank (with all other components equal to zero). Obviously, there is close correlation between the finite element results and the analytical solution, indicating that the supports at the poles and the presence of the inner tank do not significantly affect the structural response of the outer tank throughout the majority of the outer tank acreage.

Results of the preliminary MSC/NASTRAN-HyperSizer sizing of the external tank are summarized in table XIV. The table is divided into stiffened and unstiffened configurations. Recall that the weight for each design is simply the unit weight determined by the HyperSizer sizing optimization multiplied by the tank area (247 ft^2). For the unstiffened configurations, the only design parameter is the thickness, and in all four cases curved panel buckling was the controlling failure mechanism. For the grid-stiffened configurations, the four geometric design parameters are given in table XIV.

TABLE XIV.— OUTER TANK DESIGN RESULTS

Design solution	Unit weight, lb/ft^2	Weight, lb	Facesheet thickness, in.	Stiffener thickness, in.	Stiffener height, in.	Stiffener spacing, in.	Controlling failure mode	Local buckling margin
Unstiffened								
LiAl 2090	1.792	443	0.1276	–	–	–	Curved panel buckling	–
Al 2014–T6	2.133	527	0.1346	–	–	–	Curved panel buckling	–
Steel	3.896	963	0.0946	–	–	–	Curved panel buckling	–
Graphite/epoxy	1.199	296	0.1461	–	–	–	Curved panel buckling	–
Stiffened								
LiAl 2090 (bi-grid)	0.529	131	0.022	0.015	0.37	0.7	Curved panel buckling	0.1051
Al 2014–T6 (bi-grid)	0.622	153	0.018	0.019	0.36	0.5	Curved panel buckling	0.0858
Steel (iso-grid)	1.026	254	0.014	0.008	0.23	0.5	Curved panel buckling	0.0896
Graphite/epoxy (bi-grid)	0.409	101	0.0264	0.0198	0.42	0.7	Crippling-buckling interaction	0.1050

Further, the table indicates that a bi-grid configuration was chosen as the optimum for the LiAl 2090, Al 2014–T6, and graphite/epoxy materials, while for the steel material an iso-grid configuration was chosen. In addition, the controlling failure mode for the LiAl 2090, Al 2014–T6, and steel materials was curved panel buckling, while for the graphite/epoxy the controlling failure mode was crippling-buckling interaction.

The fact that local buckling was not the controlling failure mode for any of the stiffened design options is a result of using a limit load factor of safety of 1.0. The local buckling margin for each of the stiffened configurations is shown in the final column in table XIV. The minimum margin for local buckling is between 0.085 and 0.105, which (for a factor of safety of 1.0) means the local buckling load is between 8.5 and 10.5 percent below the local buckling allowable. As a result, it is obvious that if a limit load factor of safety of 1.1 were employed, local buckling would become the controlling failure mode for the stiffened aluminum and steel designs, influencing the minimum weight design for these two design options.

In terms of the weights of the outer tank designs, table XIV indicates that all stiffened configurations are lighter than all unstiffened configurations. The graphite/epoxy composite design is the lightest material choice for both the stiffened and unstiffened configurations. Given the assumptions employed in the sizing analysis outlined above, the bi-grid stiffened graphite/epoxy composite provided the lowest overall weight at 101 lb. However, the LiAl 2090 bi-grid configuration was also competitive at 131 lb, and could possibly be a better choice if the manufacturing costs (likely dominated by machining of the grid stiffeners) were significantly lower than the composite manufacturing costs.

Thermal and Structural Analysis of Sandwiched Composite Tank Design

In the thermal insulation assessment section, it was established that a vacuum-jacketed design approach provides superior thermal insulation performance over a tank design using aerogel insulation. It was established that, for a 14-day mission, the vacuum-jacketed design approach required far less additional propellant to account for boiloff, since there is far less heat penetration with the vacuum-jacketed design. A design approach using aerogel insulation, however, was shown to begin to be competitive with a vacuum-jacketed approach for shorter missions, on the order of 5 hr. For shorter duration missions, tank designs using aerogel insulation may be an attractive design solution. There is also the possibility that through advancements in aerogel engineering, aerogels with lower thermal conductivities could be developed.

One possible tank design utilizing aerogel insulation is illustrated in figure 15; it consists of a sandwiched construction using an inner and outer graphite/epoxy shell with an aerogel core. The aerogel core is bonded to both the
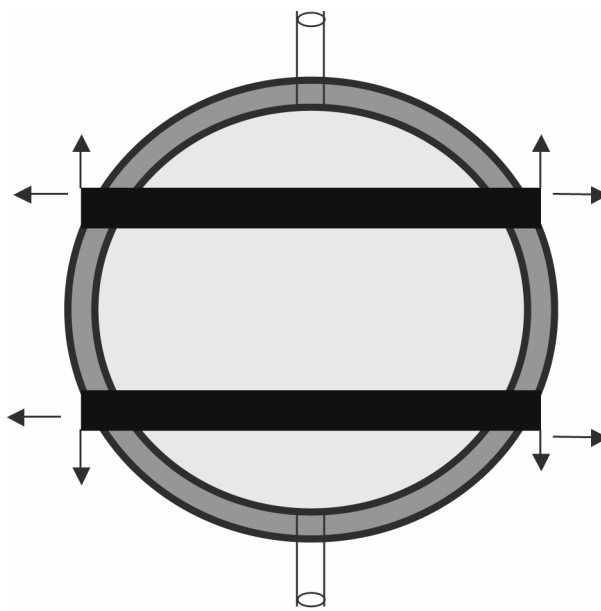

Figure 15.—Notional sketch of sandwiched composite tank with aerogel core showing metal belly bands (external) and vehicle attachment points.

inner and outer shells, providing a means for load transfer between the shells. The tank attachment to the vehicle structure could be achieved in a manner similar to that used in the vacuum-jacketed design (by routing an attachment cylinder through the outer shell and aerogel core). However, if the aerogel core has sufficient structural integrity, an alternative means of supporting the tank may be employed as illustrated in figure 15. With this approach the tank can be mounted to the vehicle structure using a set of metal bands (belly bands) with lug attachments. The belly bands will be attached with adhesive to the outer surface of the outer shell. The liquid hydrogen and tank inertial loads will be carried out through the metal band and lug arrangements. A spring or strut standoff would not be required. This approach could potentially minimize the amount and size of the penetrations for filling and draining, since the size of the penetrations would only be dictated by propellant flow requirements. This could potentially provide a benefit in reducing the amount of passive heat flow into the cryogenic tank. In addition, this approach will result in lower stresses in the inner shell near the top and bottom poles.

In addition to the thermal insulation efficiency of the aerogel, another issue that must be addressed in considering a sandwiched tank design utilizing an aerogel core is that silica aerogels possess limited tensile strength. Tensile strengths of low-density silica aerogels are less than a few pounds per square inch (ref. 3). Properties of the cross-linked silica aerogels can be tailored by modifications to the formulation, but to obtain higher strengths, the desirable properties such as low density and low thermal conductivity must be sacrificed. Of course this give-and-take requires one to know the required tensile strength of the aerogel in order to engineer materials

with the optimum set of material properties. For this purpose, a structural analysis of a sandwiched tank design was performed. The analysis attempted to determine the approximate stress magnitudes in the aerogel core under typical tank operational loads. The analysis assumes that the higher density, higher strength aerogels will be used in the core. The loads applied to the tank for this analysis are the internal and environmental pressures, the vehicle acceleration loads and the thermal loading created by the cryogenic fluid and the ambient temperature environments.

Both thermal and structural analysis of the sandwiched tank design was performed with a finite element analysis using ABAQUS (ref. 9). The thermal analysis was performed in order to provide the thermal loads to the structural analysis. The finite element model of the sandwiched tank design is shown in figure 16. The aerogel core elements are shown in green. The outer shell elements are yellow, and the inner shell elements are red. A perfect bond between the aerogel core and the adjacent shells was assumed. The liquid hydrogen was modeled explicitly and the liquid hydrogen elements are shown in black. The model consists of 55 305 elements and 28 156 nodes. Both 8-node brick and 4-node tetrahedron elements were used. In this analysis, the aerogel thickness was assumed to be 1.68 in. and the inner and outer graphite/epoxy shells were assumed to be 0.1 in. thick. The inner diameter of the inner shell was 8.53 ft.

The structural analysis was performed for two thermal environments: the steady-state thermal condition at altitude and the thermal conditions expected on the ground just prior to takeoff. The temperature distributions in the tank due to these two thermal environments were determined with thermal analyses. Both thermal analysis solutions assumed convective heating boundary conditions on the inner and outer surfaces of the sandwiched tank wall, with the inner tank surface boundary condition specified by the convection coefficient h_{conv} = 2.55×10^{-6} Btu/in^2·sec·°F and temperature T_∞ = –423 °F. For the steady-state altitude case, the convection heating boundary condition on the outer surface was specified by h_{conv} = 3.39×10^{-7} Btu/in^2·sec·°F and T_∞ = –70 °F. The thermal profile expected just prior to takeoff was determined by performing a transient analysis, which assumed an initial uniform temperature throughout the tank structure of 80 °F and imposed a convection heating boundary condition on the outer surface specified by h_{conv} = 3.39×10^{-7} Btu/in^2·sec·°F and T_∞ = 125 °F.

The material property values that were used in the thermal and structural analyses for the silica aerogel core are listed in table XV. Material property values for the silica aerogel were available at room temperature (70 °F) only, so the room-temperature property values were used for the entire range of operating temperatures. The properties listed in table XV for the silica aerogel are consistent with typical properties for the high-strength, high-density aerogel.
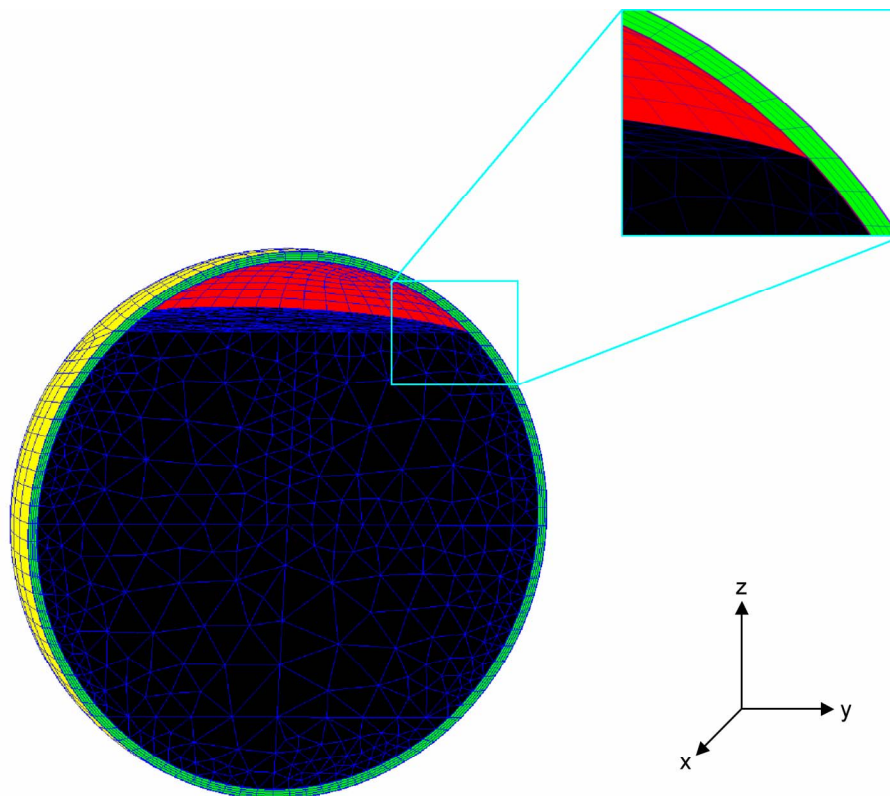

Figure 16.—Finite element mesh used for thermal and structural analyses of sandwiched tank design.

TABLE XV.—MATERIAL PROPERTIES[a] FOR POLYMER
CROSS-LINKED SILICA AEROGEL USED IN THERMAL
AND STRUCTURAL ANALYSIS OF SANDWICHED
COMPOSITE TANK

	−423 °F	−70 °F	125 °F
Density, lb/in^3	0.016	0.016	0.016
Young's modulus, ksi	10.25	10.25	10.25
Poisson's ratio	0.25	0.25	0.25
Coefficient of thermal expansion, /°F	15.8×10^{-6}	15.8×10^{-6}	15.8×10^{-6}
Thermal conductivity, Btu/in. hr·°F	1.7×10^{-3}	1.7×10^{-3}	1.7×10^{-3}
Specific heat, Btu/lb·°F	0.239	0.239	0.239

[a]From L. Capadona, 2005, NASA Glenn Research Center, Cleveland, OH, personal communication.

The material properties for the graphite/epoxy inner and outer shells are the same as those used in the graphite/epoxy inner tank analysis for the vacuum-jacketed tank design, which are listed in table VIII. The property values listed in table VIII for room temperature were also used in the current analysis as the property values for −70 and 125 °F.

The results of the two thermal analysis solutions are shown in figure 17. The transient preflight thermal profile shown in figure 17 is the profile calculated at 30 min after application of the convective heating boundary conditions. In other words, it is the thermal profile expected 30 min after filling the tank and loitering in a 125 °F ambient-temperature environment.

Two tank support arrangements were considered in the series of structural analysis solutions. These are illustrated in figure 18. One tank support arrangement used four lug attachment points (two attachment points on each belly band spaced 90° apart), and the second support arrangement used eight lug attachment points (four attachment points on each belly band spaced 90° apart). Note that the belly bands and lug attachments were not explicitly modeled in the finite element model. The restraint provided by the lug attachments were simulated by fixing the three translational degrees of freedom of the nodes located on the outer surface of the outer shell underneath the lug attachment locations. This is indicated by the pin supports shown in figure 18.

The structural analysis solution was performed to analyze the sandwiched composite tank under a variety of possible combinations of vehicle acceleration, pressurization, and thermal load conditions. A list of all the structural analysis solution load cases that were performed is shown in table XVI.
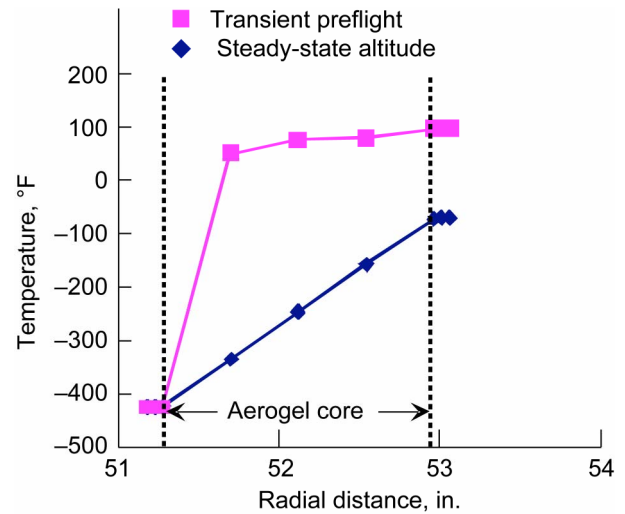

Figure 17.—Radial thermal load profile applied to sandwiched composite tank model for both preflight and altitude thermal environments.

Load cases 1 through 11 consider the possible combinations of acceleration loads and pressurization loads under the steady-state altitude thermal conditions. Load cases 1 through 7 consider the four-lug attachment arrangement, and cases 8 through 11 consider the eight-lug arrangement. Load cases 12 through 17 consider the possible load combinations under the transient preflight thermal conditions. Cases 12 through 14 consider the four-lug arrangement, and cases 15 through 17 consider the eight-lug arrangement.

Load cases 1, 8, 12, and 15 determine the stresses due to thermal loads only, whereas load cases 2, 9, 13, and 16 determine the stresses due to the combination of the thermal and pressure loads. By comparing the results from these load cases to the load cases that include the acceleration loads, the relative contribution from each of the three load sources could be determined.

The acceleration loads were applied to the model using the coordinate system shown in figure 18. Each set of acceleration loads in load cases 3 through 7 represents the combination of a 3.5g vertical acceleration load and a 0.5g lateral acceleration load directed at various lateral directions, with successive lateral directions offset by 45°. Given the presence of the lug attachment supports and restricting the choice of the lateral load directions to 45° increments, there are only five unique lateral load directions (cases 3 through 7) for the four-lug attachment arrangement. There are only two unique lateral load directions (cases 10 and 11) for the eight-lug attachment arrangement.
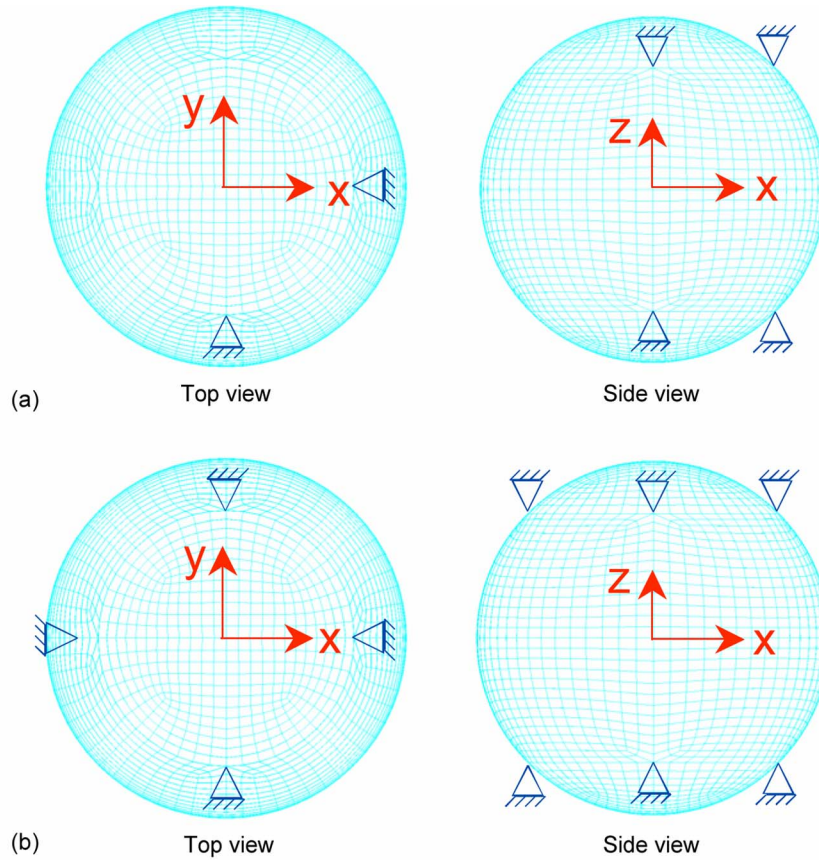
Figure 18.—Sketch illustrating the two support arrangements considered in the structural analysis of the sandwiched composite tank. (a) Four-lug attachment arrangement. (b) Eight-lug attachment arrangement.

TABLE XVI.—LOAD CASES FOR SANDWICHED COMPOSITE TANK ANALYSIS

Load case	Support attachment: number of lugs	x-direction g load	y-direction g load	z-direction g load	Internal pressure, psi	External pressure, psi
Steady-state altitude						
1	4	0.0	0.0	0.0	0.0	0.0
2	4	0.0	0.0	0.0	30.0	.8
3	4	.5	0.0	−3.5	30.0	.8
4	4	.353	.353	−3.5	30.0	.8
5	4	0.0	.5	−3.5	30.0	.8
6	4	−.353	.353	−3.5	30.0	.8
7	4	.353	−.353	−3.5	30.0	.8
8	8	0.0	0.0	0.0	0.0	0.0
9	8	0.0	0.0	0.0	30.0	.8
10	8	.5	0.0	−3.5	30.0	.8
11	8	.353	.353	−3.5	30.0	.8
Transient preflight						
12	4	0.0	0.0	0.0	0.0	0.0
13	4	0.0	0.0	0.0	30.0	14.7
14	4	.353	.353	−3.5	30.0	14.7
15	8	0.0	0.0	0.0	0.0	0.0
16	8	0.0	0.0	0.0	30.0	14.7
17	8	.353	.353	−3.5	30.0	14.7

The structural analysis results are summarized in table XVII; the maximum stress in the aerogel and in the graphite/epoxy shells is listed for each load case. Stresses in the aerogel are reported as the first principal stress, whereas in the graphite/epoxy, predicted stresses are reported as the maximum in-plane and radial (through-thickness) stresses. Note that the maximum predicted stress values in the aerogel core and both graphite/epoxy shells are quite low for all load cases. The maximum predicted principal stress in the aerogel core is less than 100 psi, orders of magnitude lower than the flexural tensile strength of the high-density aerogel as measured by Katti, et al. (ref. 14). The maximum predicted stress values for the inner and outer shells are low compared to typical strength values for graphite/epoxy (ref. 15).

TABLE XVII.—STRESS RESULTS FOR SANDWICHED TANK STRUCTURAL ANALYSIS CASES

Load case[a]	Aerogel maximum principal stress, psi	Inner tank maximum stress		Outer tank maximum stress	
		Radial, ksi	In-plane, ksi	Radial, ksi	In-plane, ksi
Steady-state altitude					
1	90.01	−5.68	3.81	0.86	−4.08
2	85.49	−.44	6.75	.23	1.21
3	89.28	−.44	7.41	.77	5.13
4	89.53	−0.45	7.44	0.80	5.18
5	89.59	−.45	7.44	.80	5.29
6	89.43	−.46	7.42	.78	5.28
7	88.99	−.44	7.37	.73	4.92
8	90.27	−0.59	3.88	0.88	−3.89
9	85.60	−.45	6.73	.26	1.43
10	85.17	−.45	6.80	.31	2.50
11	85.20	−.42	6.80	.31	2.51
Transient preflight					
12	42.47	0.29	3.08	−0.13	−2.54
13	38.64	.44	5.29	−.19	−1.84
14	42.00	.44	5.65	−.71	−5.90
15	42.50	0.29	3.09	−0.13	−2.55
16	38.68	.44	5.29	−.19	−1.83
17	38.56	.42	5.25	−.22	−2.89

[a]See table XVI for load case descriptions.

In comparing the maximum stress values for the thermal-only load cases to those load cases that include pressure and acceleration loads, it appears that the thermal loads are the most significant source of loading, particularly in regard to the aerogel stresses. Since the thermal loads are the most significant source, it is not surprising that the maximum predicted stress values are low for all load cases. The aerogel modulus and the coefficient of thermal expansion of the graphite/epoxy composite, the two primary material properties that dictate the thermal stresses, are low.

It should also be noted that the location of the maximum stresses listed in table XVII for the aerogel, the inner tank, and the outer tank are all in the vicinity of the lug attachment supports. This is illustrated in figure 19, where the stress contours in the aerogel core and the outer shell are plotted for load case 4. It is expected that if the metal band and lug attachments were to be modeled explicitly, a more precise simulation of the load transfer from the tank through the metal bands and lug attachments and out to the vehicle attachment points would be achieved. The loads carried through the lug attachments would be distributed over a larger area of the outer tank, and the predicted stresses in the aerogel and the inner and outer shells would be less than that predicted with the current analysis. As a result, the stresses in the aerogel and in the inner and outer shells listed in table XVI are higher than the maximum expected stresses during these load cases.

Permeation Studies: Establishing Permeability Limits

Permeation through the graphite/epoxy tank wall must be considered because it may prohibit the use of graphite/epoxy composites in either vacuum-jacketed or sandwiched tank designs. In order to establish material permeability limits for tank designs proposing the use of graphite/epoxy composites, a series of flow calculations were performed. The flow calculations were based on the assumption that the flow mechanism is viscous flow through a porous solid. These calculations were based on the solution of Darcy's law. Using Darcy's law, the fluid mass flux vector $\mathbf{J}$ is written as

$$\mathbf{J} = \rho\mathbf{v} = \frac{-\rho}{\mu}\mathbf{k}\cdot\nabla P \qquad (2)$$

where $\mathbf{v}$ is the average velocity vector of the diffusing fluid, ρ is the density of the diffusing fluid, $\mathbf{k}$ is the second-order material permeability tensor, μ is the viscosity of the fluid, P is the fluid pressure, and ∇ is the gradient operator. The negative sign is present in equation (2) since the direction of the mass flux vector is always opposite to the direction of the pressure gradient.

Equation (2) was applied to calculate the flow rates for the diffusion of ambient air through the outer tank as well as the diffusion of liquid hydrogen through the inner tank. The problem description is illustrated in figure 20. Both flow mechanisms will cause an increase in the pressure in the vacuum gap. This is potentially a problem in both vacuum-jacketed designs or in sandwiched designs using an aerogel core under vacuum. In the remainder of this section, any reference to a vacuum gap includes either the vacuum space between the tanks in a vacuum-jacketed design or the volume occupied by the aerogel in a sandwiched design. Flow through the walls and the accumulation of gases into either space could potentially lead to a variety of issues, most notably a marked increase in thermal conductivity.
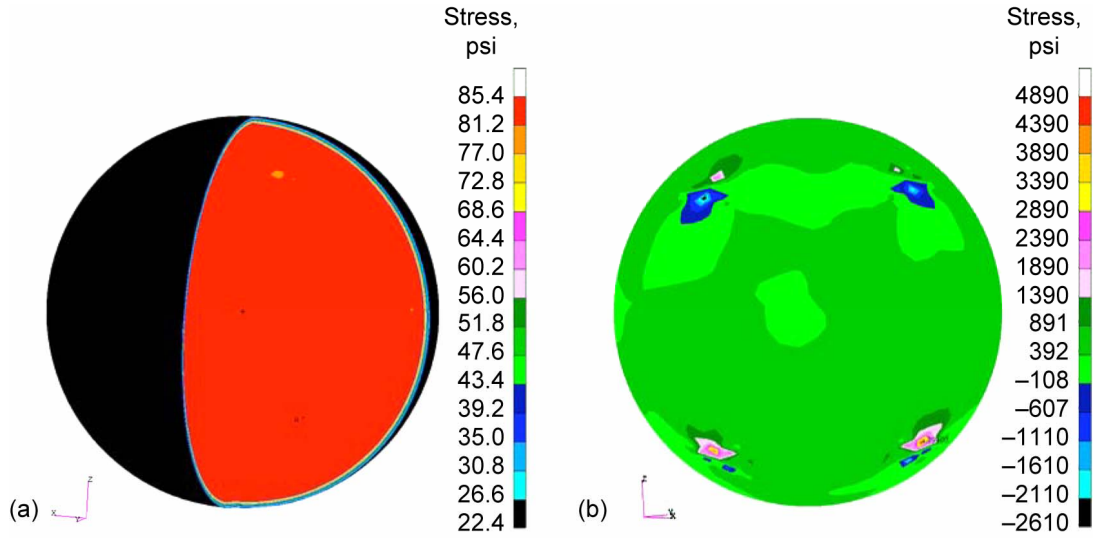
Figure 19.—Stress contour plots in aerogel core and outer shell of sandwiched composite tank for load case 4 (see table XVI for case description). (a) Aerogel core. (b) Outer shell.
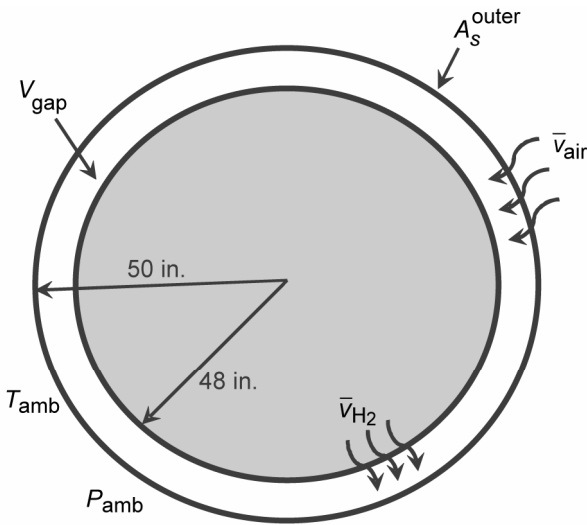

Figure 20.—Problem definition to assess permeation through graphite/epoxy walls in either vacuum-jacketed or sandwich tank designs. A_S^{outer} is surface area of outer tank; V_{gap}, volume of vacuum gap; $\bar{v}_{air}$, average velocity of air; $\bar{v}_{H_2}$, average velocity of liquid hydrogen; T_{amb}, ambient temperature; and P_{amb}, ambient pressure.

Assuming that the fluid pressures act uniformly around the tank wall surfaces, the only nonzero pressure gradient is the radial pressure gradient. As such, the only nonzero fluid mass flux is a radial flux, which will also be uniform around the tank surface. The mass flux magnitude is given by

$$J = |\mathbf{J}| = \rho \frac{k}{\mu} \frac{\partial P}{\partial r} \tag{3}$$

where k is the graphite/epoxy permeability in the tank thickness direction and $\partial P / \partial r$ is the radial pressure gradient.

The mass continuity equation defines the time rate of change of gas density in the vacuum gap in terms of the mass flux through the tank wall as

$$\frac{d\rho_{gap}}{dt} = J \frac{A_s}{V_{gap}} \tag{4}$$

where A_s is the surface area of the tank and V_{gap} is the volume of the vacuum gap.

It is assumed that when either fluid (air or liquid hydrogen) enters the vacuum gap, the diffusing specie behaves as an ideal gas; thus the time derivative form of the ideal gas law can be used to express the rate of change of pressure in the vacuum gap in terms of the time rate of change of gas density in the vacuum gap:

$$\frac{dP_{gap}}{dt} = \frac{RT}{M} \frac{d\rho_{gap}}{dt} \tag{5}$$

where R is the universal gas constant and M is the molecular weight of the diffusing fluid. Combining equations (3), (4), and (5) leads to

$$\frac{dP_{gap}}{dt} = \frac{RT}{M} \rho \frac{k}{\mu} \frac{\partial P}{\partial r} \frac{A_s}{V_{gap}} \tag{6}$$

Equation (6) was applied to assess three cases; these are specified in table XVIII. The first two cases address the flow of ambient air inward through the outer tank and represent the ground operations and altitude conditions. The third case addresses the flow of liquid hydrogen outward through the

TABLE XVIII.—PARAMETERS FOR FLOW ANALYSES

Parameters	Case 1	Case 2	Case 3
Diffusing fluid	Ambient air	Ambient air	Liquid hydrogen
Temperature of diffusing fluid, T, °F	125	−70	−423
Pressure, P, psi	14.7	0.8	30
Molecular weight of diffusing fluid, M, g/g·mole	28.8	28.8	2
Density of diffusing fluid, ρ, lb/ft^3	[a]0.0674	[a]0.00551	[b]4.4179
Viscosity of diffusing fluid, μ, lbf·s/ft^2	[c]4.177×10^{-7}	[c]3.342×10^{-7}	[b]2.297×10^{-7}
Surface area of tank,[d] A_s, in^2	31 416	31 416	28 953
Volume of vacuum gap,[e] V_{gap}, in^3	60 352	60 352	60 352

[a]Calculated using the ideal gas law, $\rho = PM/RT$.
[b]From reference 16.
[c]Extrapolated or interpolated from data tables listed in reference 17.
[d]Calculated using $A_s = 4\pi r^2$, where r is tank radius.
[e]Calculated using $V_{gap} = 4\pi(r_o^3 - r_i^3)/3$, where r_o and r_i are outer and inner tank radii, respectively.

inner tank. The values for the density and viscosity of liquid hydrogen were obtained from reference 16. The values of the viscosity of air at the case temperatures were obtained by extrapolation and interpolation from data tables in reference 17.

Since air may be assumed to behave as an ideal gas, equation (6) may be rewritten for the first two cases using the ideal gas law ($P = \rho RT/M$) as

$$\frac{dP_{gap}}{dt} = P_{amb} \frac{k}{\mu} \frac{P_{amb}}{h} \frac{A_s}{V_{gap}} \qquad (7)$$

where P_{amb} is the pressure of the ambient air external to the tank. In addition, the pressure gradient $\partial P/\partial r$ in equation (6) has been replaced by P_{amb}/h, where h is the thickness of the tank wall. In applying equation (6) to assess case 3 (liquid hydrogen permeation through the inner tank or shell), the ideal gas law does not apply and the pressure gradient is calculated as the internal pressure (30 psi) divided by the assumed inner tank wall thickness.

Using equations (6) and (7) and the values for the problem parameters listed in table XVIII, a plot of the rate of change of vacuum gap pressure versus the graphite/epoxy permeability can be drawn for the three cases under consideration. This is shown in figure 21. Results are shown for assumed tank wall thicknesses of 0.1 and 0.15 in. Figure 21 indicates that for vacuum gap pressure rise rates less than 0.1 psi/day (1 psi over a 10-day mission), the material permeability of the outer tank cannot be greater than 1.55×10^{-15} in^2 (case 2). Using the same vacuum gap pressure rise rate, the permeability of the inner tank cannot exceed 1.55×10^{-20} in^2 (case 3). The results shown for case 1 are somewhat inconsequential, since this is the case associated with preflight ground operations and since the time duration for preflight operations is expected to be a small fraction of the total mission duration. The results for case 1 are included to show the effect of temperature and ambient air pressure.

It is obvious from the plots in figure 21 that case 3, the diffusion of liquid hydrogen through the inner tank, is a more stringent case for setting permeability requirements on graphite/epoxy composites. That is, for any given rate of vacuum loss, case 3 will always require the lowest permeability value. This is the result of the higher density, lower molecular weight, and lower viscosity values of liquid hydrogen compared to those of air.

Discussion of Results

In the assessment of the various thermal insulation approaches, it was established that a vacuum-jacketed design with an MLI blanket offered the most efficient thermal insulation design option. A tank design using SOFI, or either high-strength or low-strength aerogels results in a much heavier tank system, due to a higher rate of heat penetration and more propellant boiloff. As such, aerogels are not a viable insulation option for the long-term storage of cryogenic hydrogen. They may, however, be a candidate for shorter duration missions.

Structural analysis of the vacuum-jacketed design was performed to determine the minimum inner tank thickness (and inner tank weight) required to maintain a positive margin of safety under operational conditions. Minimum weights were determined for both an aluminum inner tank and a graphite/epoxy inner tank. For an aluminum inner tank, the minimum inner tank wall thickness was found to be 0.031 in. and the minimum support rod wall thickness was found to be 0.17 in., resulting in a combined weight for the tank, connecting rings, and support rod of 128 lb. For the graphite/epoxy tank, the minimum required inner tank wall thickness was found to be 0.06 in. Using two 12-in.-long support tubes, with a wall thickness of 0.1 in. and a diameter of 4 in. on both poles, a combined weight for the tank and support tubes of 118 lb was obtained. Thus, the application of nanoclay-enhanced graphite/epoxy as an inner tank would result in a weight savings of only 10 lb.
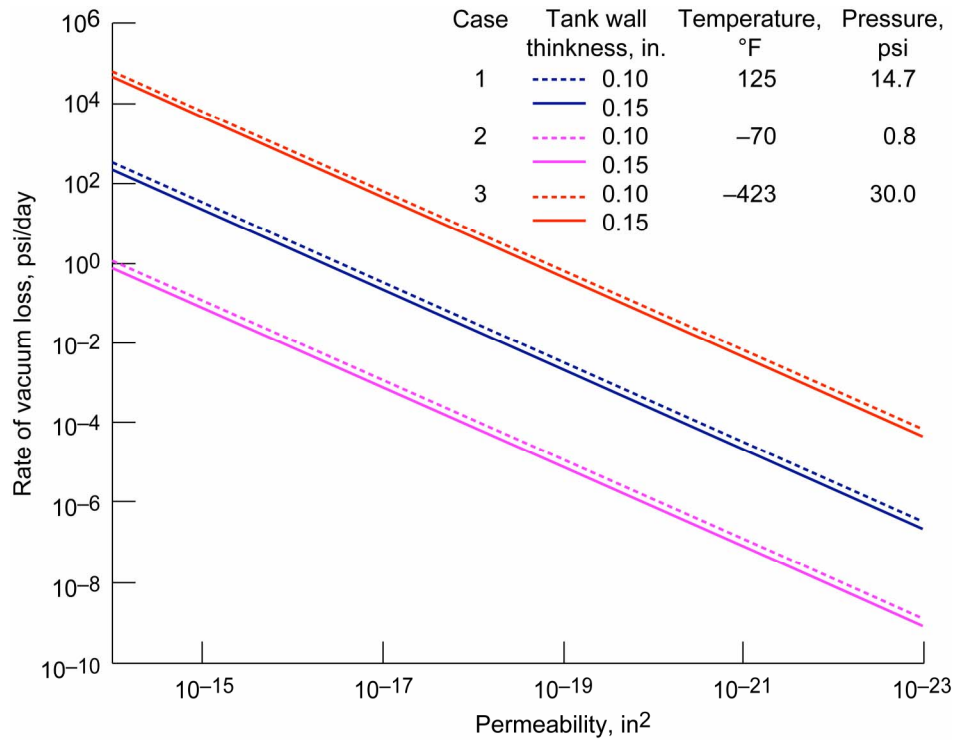
Figure 21.—Rate of vacuum loss versus graphite/epoxy permeability.

The outer tank design was determined through buckling analysis of potential designs and the application of the HyperSizer optimization software. It was determined that a graphite/epoxy with a bi-grid stiffened construction offered the minimum weight outer tank design option. The weight of a graphite/epoxy tank using a bi-grid stiffened construction was calculated to be 101 lb. The second lightest tank design candidate was a bi-grid-stiffened aluminum-lithium tank, with an estimate weight of 131 lb.

The thermal and structural analysis of a sandwiched tank design with an aerogel core revealed that the expected maximum principal stress in the aerogel core due to typical in-service loads is approximately 100 psi. This value is well within the tensile strength limits of the high-density aerogel. The predicted low aerogel stress value is due primarily to the low coefficient of thermal expansion of the graphite/epoxy inner shell and the low modulus of the aerogel.

By performing flow calculations using Darcy's law, the rate at which the vacuum gap (or the vacuum space in an evacuated aerogel) is pressurized was determined as a function of material permeability. This allows one to set material permeability limits for inner and outer tanks/shells. In order to limit the vacuum pressure rise rate to less than 0.1 psi/day, it was determined that the permeability of the outer wall should not exceed 1.55×10^{-15} in^2 and the permeability of the inner tank should not exceed 1.55×10^{-20} in^2.

The permeability of nanoclay-enhanced graphite/epoxy specimens has recently been measured by S. Miller (2005, NASA Glenn Research Center, Cleveland, OH, unpublished results). An average value slightly less than 1.55×10^{-20} in^2 was obtained. This would indicate that the current nanoclay-enhanced graphite/epoxy possesses a permeability value low enough to limit liquid hydrogen diffusion and keep vacuum gap pressure rise rates below 0.1 psi/day. Certainly, a value of 1.55×10^{-20} in^2 is low enough to give nanoclay-enhanced graphite/epoxy consideration for outer tank applications. Keep in mind, however, that this permeability value was measured during tests conducted on unstressed, pristine (not thermally cycled) specimens.

Concluding Remarks

The analyses presented herein were conclusive in establishing the thermal insulating superiority of a vacuum-jacketed design over high- or low-density aerogel or spray-on foam insulation designs. One is left with the conclusion that an aerogel is not a viable design solution for a 14-day mission. As for the nanoclay-enhanced graphite/epoxy, these materials do possess sufficiently low material permeability to be considered possible candidate materials for the construction of inner or outer tanks in a vacuum-jacketed design approach.

The reader should be cautioned, however, to recognize that this analysis assessment did not include an assessment of the internal stresses in the graphite/epoxy composite generated at low temperatures due to the thermal expansion mismatch between the fibers and the matrix. This will lead to material damage and the increase in material permeability. This could

potentially have a detrimental effect on nanoclay-enhanced graphite/epoxy composites in either an inner tank or outer tank application.

Future work should include an analysis of the internal stresses due to cryogenic thermal cycling and the thermal expansion mismatch between the fibers and matrix to assess the potential for damage and the subsequent increase in material permeability. This should be accompanied by a parallel experimental effort to measure any increase in material permeability with thermal cycling.

There is also another matter regarding the minimum number of plies required to develop the material permeability. Specifically, the analysis of the graphite/epoxy inner tank showed that a thickness of 0.06 in. was sufficient to meet the required structural safety factors under operational loads. Given a typical ply thickness of 5 to 10 mils, a tank wall thickness of 0.06 in. could be achieved with 6 to 12 plies. The question remains as to whether the tank walls can be fabricated with only six plies and still develop the permeation resistance needed to contain the liquid hydrogen. Future work should also include an experimental effort to determine the minimum number of plies required to obtain a material permeability low enough to meet the design requirements.

All things considered, it appears that the most promising candidate for the long-term storage of cryogenic hydrogen and one that offers the greatest potential for minimizing weight while meeting all tank design requirements is a vacuum-jacketed design approach utilizing an aluminum inner tank, a bi-grid-stiffened nanoclay-enhanced graphite/epoxy outer tank, and a multilayer insulation blanket in the vacuum space.

Glenn Research Center
National Aeronautics and Space Administration
Cleveland, Ohio, April 2006

References

1. United States Air Force. http://www.af.mil/ Accessed Mar. 16, 2006.
2. Civil UAV Capability Assessment Workshop, University of Akron, Akron, OH, Apr. 2005. http://www.innovationlabs.com/uav3/ Accessed Mar. 16, 2006.
3. Frozen Smoke. NASA Marshall Space Flight Center, June 27, 1997. http://science.nasa.gov/newhome/headlines/msad05mar97_1.htm Accessed Mar. 16, 2006.
4. Federal Aviation Administration Regulation. FAR section 27.303. http://www.flightsimaviation.com/data/FARS/part_27-303.html Accessed Mar. 16, 2006.
5. Thermal Properties of Silica Aerogels. Ernest Orlando Lawrence Berkeley National Laboratory. http://eande.lbl.gov/ECS/aerogels/satcond.htm Accessed Mar. 16, 2006.
6. Johnson, Theodore F., et al.: Cryopumping in Cryogenic Insulations for a Reusable Launch Vehicle. Proceedings of the International SAMPE Symposium and Exhibition, vol. 48, 2003, pp. 731–745.
7. Barron, Randall F.: Cryogenic Systems. Oxford University Press, New York, NY, 1985.
8. MSC.Nastran 2005—Installation and Operations Guide. MSC.Software Corporation, Santa Ana, CA, 2005.
9. ABAQUS/Standard. Finite Element Program. Version 6.5–1 (c), Hibbitt, Karlsson & Sorenson, Inc., Pawtucket, RI, 2005.
10. Murthy, Pappu L.N.; Ginty, Carol A.; and Sanfeliz, Jose G.: Second Generation Integrated Composite Analyzer (ICAN) Computer Code. NASA TP–3290, 1993.
11. Peterson, J.P.; Seide, P.; and Weingarten, V.I.: Buckling of Thin-Walled Circular Cylinders. NASA SP–8007, 1968.
12. Collier, Craig; and Yarrington, Phil: Consistent Structural Integrity in Preliminary Design Using Experimentally Validated Analysis. AIAA–2005–2366, 2005, pp. 6785–6814.
13. Collier, Craig; Yarrington, Phil; and Van West, Barry: Composite, Grid-Stiffened Panel Design for Post Buckling Using HyperSizer. AIAA–2002–1222, 2002.
14. Katti, A., et al.: Chemical, Physical, and Mechanical Characterization of Isocyanate Cross-Linked Amine-Modified Silica Aerogels. Chem. Mater., vol. 18, no. 2, 2006, pp. 285–296.
15. The Composite Materials Handbook. MIL–HDBK–17–2F, vol. 2, ASTM International, West Conshohocken, PA, 2002.
16. Weast, Robert C., ed.: CRC Handbook of Chemistry and Physics: A Ready-Reference Book of Chemical and Physical Data. 64th ed., CRC Press, Boca Raton, FL, 1983.
17. Avallone, Eugene A.; and Baumeister III, Theodore, eds.: Marks' Standard Handbook for Mechanical Engineers. Ninth ed., McGraw-Hill Book Company, New York, NY, 1987.

REPORT DOCUMENTATION PAGE

1. AGENCY USE ONLY (Leave blank)	2. REPORT DATE	3. REPORT TYPE AND DATES COVERED
	May 2006	Technical Paper

4. TITLE AND SUBTITLE

Engineering Analysis Studies for Preliminary Design of Lightweight Cryogenic Hydrogen Tanks in UAV Applications

5. FUNDING NUMBERS

WBS 599489.02.07.03

6. AUTHOR(S)

Roy M. Sullivan, Joseph L. Palko, Robert T. Tornabene, Brett A. Bednarcyk, Lynn M. Powers, Subodh K. Mital, Lizalyn M. Smith, Xiao-Yen J. Wang, and James E. Hunter

7. PERFORMING ORGANIZATION NAME(S) AND ADDRESS(ES)

National Aeronautics and Space Administration
John H. Glenn Research Center at Lewis Field
Cleveland, Ohio 44135–3191

8. PERFORMING ORGANIZATION REPORT NUMBER

E–15431

9. SPONSORING/MONITORING AGENCY NAME(S) AND ADDRESS(ES)

National Aeronautics and Space Administration
Washington, DC 20546–0001

10. SPONSORING/MONITORING AGENCY REPORT NUMBER

NASA TP—2006-214094

11. SUPPLEMENTARY NOTES

Roy M. Sullivan, Robert T. Tornabene, Lizalyn M. Smith, Xiao-Yen J. Wang, and James E. Hunter, Glenn Research Center; Joseph L. Palko, Connecticut Reserve Technologies, Inc., 10030 Greenwich Dr., Strongsville, Ohio 44136; Brett A. Bednarcyk and Lynn M. Powers, Ohio Aerospace Institute, 22800 Cedar Point Road, Brook Park, Ohio 44142; Subodh K. Mital, University of Toledo, 2801 W. Bancroft St., Toledo, Ohio 43606. Responsible person, Roy M. Sullivan, organization code RXL, 216–433–3249.

12a. DISTRIBUTION/AVAILABILITY STATEMENT

Unclassified - Unlimited
Subject Category: 07

Available electronically at http://gltrs.grc.nasa.gov

This publication is available from the NASA Center for AeroSpace Information, 301–621–0390.

12b. DISTRIBUTION CODE

13. ABSTRACT (Maximum 200 words)

A series of engineering analysis studies were conducted to investigate the potential application of nanoclay-enhanced graphite/epoxy composites and polymer cross-linked silica aerogels in cryogenic hydrogen storage tank designs. This assessment focused on the application of these materials in spherical tank designs for unmanned aeronautic vehicles with mission durations of 14 days. Two cryogenic hydrogen tank design concepts were considered: a vacuum-jacketed design and a sandwiched construction with an aerogel insulating core. Analyses included thermal and structural analyses of the tank designs as well as an analysis of hydrogen diffusion to specify the material permeability requirements. The analyses also provided material property targets for the continued development of cross-linked aerogels and nanonclay-enhanced graphite/epoxy composites for cryogenic storage tank applications. The results reveal that a sandwiched construction with an aerogel core is not a viable design solution for a 14-day mission. A vacuum-jacketed design approach was shown to be far superior to an aerogel. Aerogel insulation may be feasible for shorter duration missions. The results also reveal that the application of nanoclay-enhanced graphite/epoxy should be limited to the construction of outer tanks in a vacuum-jacketed design, since a graphite/epoxy inner tank does not provide a significant weight savings over aluminum and since the ability of nanoclay-enhanced graphite/epoxy to limit hydrogen permeation is still in question.

14. SUBJECT TERMS

Aerogels; Graphite epoxy composites; Structural analysis; Thermal analysis; Finite element method; Permeability; Thermal insulation; Cryogenic hydrogen storage tanks; Nanoclay composites

15. NUMBER OF PAGES

32

16. PRICE CODE

17. SECURITY CLASSIFICATION OF REPORT	18. SECURITY CLASSIFICATION OF THIS PAGE	19. SECURITY CLASSIFICATION OF ABSTRACT	20. LIMITATION OF ABSTRACT
Unclassified	Unclassified	Unclassified	